JOURNAL OF GEOPHYSICAL RESEARCH, VOL. 113, E08002, doi:10.1029/2007JE002980, 2008

Strike-slip faults on Mars: Observations and implications for global tectonics and geodynamics

Jeffrey C. Andrews-Hanna,[1] Maria T. Zuber,[1] and Steven A. Hauck II[2]

Received 6 August 2007; revised 16 January 2008; accepted 1 May 2008; published 5 August 2008.

[1] The tectonic evolution of Mars has been driven primarily by the interaction of Tharsis-induced loading stresses with a uniform contractional stress field, leading to global assemblages of graben and wrinkle ridges. Until recently, strike-slip faults have appeared to be largely absent from the tectonic record. We here present evidence for a new set of Noachian to Early Hesperian strike-slip faults southwest of Tharsis. The best-preserved fault in the newly mapped set has a length of ~200 km and measured lateral offset of 5–9 km. We use the locations of both previously mapped and newly identified strike-slip faults to investigate the tectonic and geodynamic evolution of Mars. We model the tectonic evolution of the planet in response to the evolving balance between the loading and contractional stresses, finding widespread regions in which strike-slip faulting was favored. The observed tectonic history is consistent with a scenario in which loading-induced stresses peaked early in Mars history, followed by the growth of contractional stresses, leading to a shift in the preferred locus of strike-slip faulting from regions southwest of Tharsis in the Noachian to Early Hesperian, to northwest of Tharsis in the Early Amazonian. The contractional strain history inferred from the ages and locations of the strike-slip faults is consistent with the strains calculated from models of the thermal evolution of Mars in which the gradual secular cooling of the planet over time was augmented by plume-induced contraction during Tharsis formation in the Noachian.

Citation: Andrews-Hanna, J. C., M. T. Zuber, and S. A. Hauck II (2008), Strike-slip faults on Mars: Observations and implications for global tectonics and geodynamics, *J. Geophys. Res.*, *113*, E08002, doi:10.1029/2007JE002980.

1. Introduction

[2] The surface record of tectonism on Mars provides the best clues to the global geodynamic evolution. While faulting on the Earth is driven largely by plate tectonic stresses as a result of a mobile lithosphere, Mars is a single plate planet on which faulting has occurred primarily in response to loading of the lithosphere and global contraction as a result of the secular cooling of the planet. The Tharsis rise, a volcanic province covering roughly 15% of the surface of the planet with an elevation above the surrounding terrain of roughly 8 km, has dominated the global stress field and resultant tectonism. The role of Tharsis in the tectonic evolution of the planet was recognized early [e.g., *Banerdt et al.*, 1982; *Carr*, 1974; *Sleep*, 1994] as a result of the global assemblage of radial graben and circumferential wrinkle ridges centered on the rise (Figure 1).

[3] Inversion of the gravity and topography of Mars demonstrated that the radial graben surrounding Tharsis are best explained by the stresses generated by membrane-flexural support of the rise [*Banerdt et al.*, 1992]. Recent refinements in our knowledge of the Martian topography and gravity fields from the Mars Orbiter Laser Altimeter instrument (MOLA) [*Smith et al.*, 2001, 1999b] and tracking of the Mars Global Surveyor spacecraft [*Smith et al.*, 1999a] resulted in an improved fit of the loading-induced stress field with the orientations of the radial graben outside of Tharsis [*Banerdt and Golombek*, 2000]. However, the continuation of the graben onto the Tharsis rise through regions of predicted strike-slip and thrust faulting would require an early period of intrusive uplift [*Phillips et al.*, 1990], the presence of a detached crustal cap over Tharsis [*Tanaka et al.*, 1991], or perhaps added stress from dikes beneath the graben [*Ernst et al.*, 2001; *Schultz et al.*, 2004a; *Wilson and Head*, 2002].

[4] While the tectonic history of Mars has clearly been dominated by the Tharsis-induced flexural and membrane stresses, loading alone cannot account for the full suite of tectonic features surrounding the rise. The population of wrinkle ridges superimposed over and apparently contemporaneous with the graben are generally accepted to be the surface manifestation of thrust faults, and require an additional compressive stress field [*Golombek et al.*, 2001; *Watters*, 1993]. Furthermore, there is growing evidence for strike-slip faults on Mars [*Forsythe and Zimbelman*, 1989; *Schultz*, 1989; *Anguita et al.*, 2001; *Tanaka et al.*, 2003; *Artita and Schultz*, 2005; *Okubo and Schultz*, 2006],

[1]Department of Earth, Atmospheric, and Planetary Sciences, Massachusetts Institute of Technology, Cambridge, Massachusetts, USA.
[2]Department of Geological Sciences, Case Western Reserve University, Cleveland, Ohio, USA.

0148-0227/08/2007JE002980$09.00

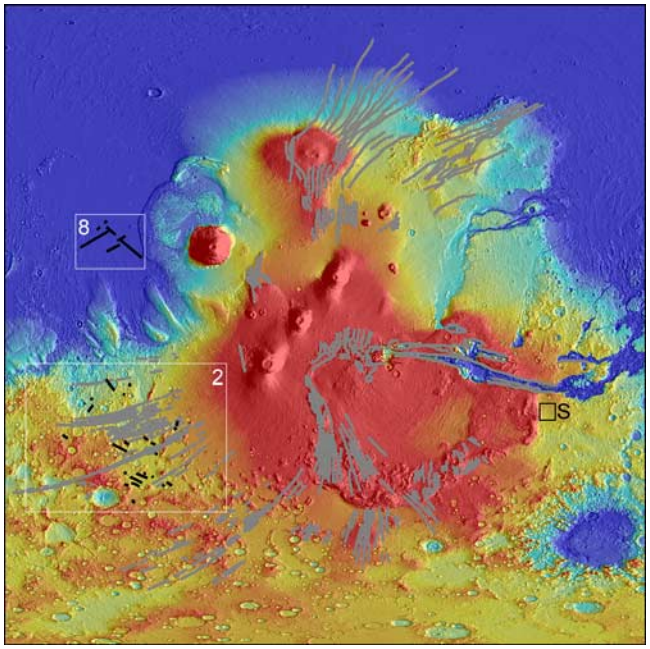

Figure 1. Partial map of graben (gray) and strike-slip faults (black) surrounding the Tharsis rise, including the proposed strike-slip faults of this study (map in cylindrical projection between ±75°N and between 180°E and 330°E). The strike-slip faults identified by *Schultz* [1989] are located within the black box (labeled "S"). The locations of Figures 2 and 8 are shown for context.

but their locations conflict with the loading models, which predict normal faulting in these regions. The presence of an additional global horizontally compressive stress field driven by the contraction of the planet has been invoked to explain the compressional tectonism [*Golombek et al.*, 2001; *Watters*, 1993], and would likely have affected the formation of strike-slip faults as well, but the detailed interaction of this contractional stress field with the loading-induced stresses has not been investigated. These global contractional stresses reflect the internal and thermal evolution of the planet, and thus understanding the tectonic evolution of Mars may shed light on the global history of geodynamics.

[5] We here consider the tectonic and geodynamic evolution of Mars, focusing on the record of strike-slip faulting as an indicator of the global stress state. We first present evidence for a new set of ancient strike-slip faults southwest of Tharsis, and reexamine evidence for strike-slip faults northwest of Tharsis. We then investigate the tectonic evolution of Mars under the combined influence of both the loading-induced flexural and membrane stresses around Tharsis, and an assumed contractional stress field, resulting in predicted tectonic styles that differ substantially from the loading model alone. The predictions of the models are compared with the locations and ages of both the previously documented and newly identified strike-slip faults, allowing us to place constraints on the loading and contractional histories. The calculated contractional strains are then compared with theoretical estimates, based on the effects of both secular cooling and plume-induced contraction of the planet during Tharsis formation.

2. Tectonic Evidence

2.1. Mars Tectonic History Overview

[6] We first review the current understanding of the tectonic evolution of the Tharsis region. *Anderson et al.* [2001] divide the tectonic history of Mars into five stages. The greatest number of tectonic features formed during stage 1 tectonism in the Noachian (alternately, the Syria-centered tectonism of *Plescia and Saunders* [1982]), including extensional faulting high on the Tharsis rise as well as the formation of a large number of the radial dike-induced graben. This peaking of Tharsis-related tectonism suggests that the bulk of Tharsis construction occurred at this time, and the approximate agreement of the orientations of the stage 1 graben with those that formed later and with the predictions of loading models suggests that the general form of the Tharsis load has not changed significantly since the Noachian [*Banerdt and Golombek*, 2000]. Further extensional tectonism occurred in the Late Noachian and Early Hesperian during stage 2, though this activity was confined largely to the Valles Marineris canyons and the regions to the east and south of Tharsis. Dike-induced graben formation to the west of Tharsis continued during stage 3 in the Hesperian. Stage 4 and 5 extensional tectonism was localized primarily around the Tharsis Montes and other volcanic constructs on the rise, with comparatively little activity west of Tharsis.

[7] The majority of the wrinkle ridges are attributed to stage 3 tectonism during the Hesperian, though stratigraphic relationships [*Dohm and Tanaka*, 1999] and the diffuse tectonic centers defined by the wrinkle ridge orientations [*Anderson et al.*, 2001] suggest a prolonged period of wrinkle ridge formation dating back to the Noachian. The distribution of wrinkle ridges in the northern lowlands [*Head et al.*, 2002] indicates that compressional tectonism continued into the Early Amazonian [*Tanaka et al.*, 2003].

2.2. Significance and Identification of Strike-Slip Faults

[8] We here focus on strike-slip faults, rather than the oft-studied radial graben, as a record of the stress history of the Martian lithosphere. While the graben surrounding the Tharsis rise are generally ascribed to be the result of Tharsis loading-induced stresses, it is thought that many of the graben are underlain by giant dike swarms [*Ernst et al.*, 2001; *Schultz et al.*, 2004a; *Wilson and Head*, 2002] and thus cannot be treated as purely tectonic features. At the point of their initiation, the dikes will be oriented orthogonal to the σ_3 direction (where we adopt the convention of the greatest compressive principal stress being defined as σ_1, with $\sigma_1 > \sigma_2 > \sigma_3$). However, once established, the effects of the magma pressure and the focusing of the dike-induced stress at the propagating dike tip will allow the dikes to continue to propagate through regions of predicted strike-slip or thrust faulting, with the dikes oriented perpendicular to the least horizontal compressive stress (σ_3 or σ_2, respectively), allowing σ_1 to be oriented either vertically or along the direction of propagation. Thus while radial graben can be used to uniquely identify the orientations of the least and

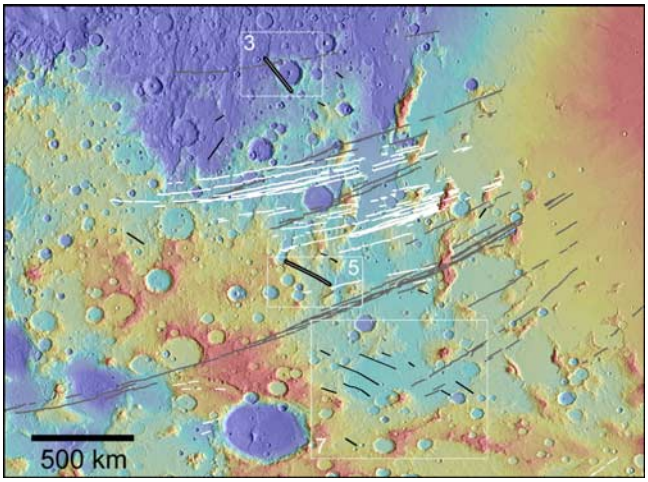

Figure 2. Map of potential strike-slip faults (black) west of Tharsis compared with the locations of stage 1 (white) and stage 3 (gray) graben. The proposed faults for which a more compelling case can be made in favor of a strike-slip interpretation are shown by double lines. Boxes show context for Figures 3, 5, and 7.

greatest horizontal stresses, they do not constrain the relative magnitude of the vertically oriented principal stress vector or the preferred style of nonmagmatic tectonism in a region. The addition of a uniform horizontal compressive stress field as a result of global contraction will not affect the orientation of either the least horizontal compressive stress or the dike-induced graben, and thus the graben are of only limited usefulness in constraining the stress state of Mars at the time of their formation.

[9] In contrast, strike-slip faults are affected only by the regional stress field, and will form only in regions where both σ_1 and σ_3 are oriented horizontally, with the faults at an angle of roughly 30° from the σ_1 direction. Similarly, the thrust faults thought to underlie the wrinkle ridges will form only when σ_1 and σ_2 are horizontal, with the surface trace of the ridge perpendicular to the σ_1 direction. Fault development also requires that the deviatoric stresses exceed some critical stress based on the strength of the rocks [*Schultz and Zuber*, 1994]. Thus the presence and orientation of strike-slip faults and wrinkle ridges provides a unique diagnostic of the orientations of all three principal stress directions as well as a limit on the magnitude of the deviatoric stress, allowing us to place constraints on the stress state of Mars at the time of their formation. The history of wrinkle ridge formation is difficult to constrain, as a result of their ubiquitous distribution and the difficulty in determining the age of the onset of wrinkle ridge formation in a given area. For this reason, we focus on the distribution and ages of strike-slip faults.

[10] Early studies noted a lack of evidence for strike-slip faults on Mars in the regions adjacent to Tharsis, in conflict with the simple loading models [e.g., *Sleep and Phillips*, 1985]. However, the identification of ancient strike-slip faults on Mars can be difficult. Terrestrial strike slip faults are readily identified by their large lateral offsets, a condition made possible by the mobile lithosphere created by plate tectonics. Mars, on the other hand, is a single-plate planet in which such large lateral offsets are not possible as a result of the pinning of the faults at their ends. Isolated (intraplate) terrestrial faults follow a linear relationship between total fault displacement (D) and fault length (L), with a D:L ratio of approximately 3×10^{-2} [*Scholz*, 2002]. As displacement accumulates on the faults, the stresses are focused at the fault tips, which propagate along-strike until the stresses no longer exceed the rock strength. Some workers have suggested a lower D:L ratio on Mars of $\sim 6 \times 10^{-3}$, as a result of the effect of the lower Martian gravity on the driving stresses and the strength of the lithosphere [*Schultz et al.*, 2004b]. However, a recent study of normal faults on Mars found a D:L ratio more similar to the terrestrial value [*Hauber et al.*, 2007]. Thus a 100-km long strike-slip fault on Mars would be expected to have a displacement of only 0.6 to 3.0 km. For ancient strike-slip faults, the extensive impact gardening of the surface [*Hartmann et al.*, 2001], heightened early erosion rates [*Golombek et al.*, 2006], and volcanic resurfacing could easily obscure the evidence for such modest offsets. Thus Noachian- and Hesperian-aged faults may be more easily identified by their overall morphology than by the lateral offsets.

[11] The trace of a fault may be visible as either a positive or negative relief feature, as a result of the effect of faulting on the strength of the rocks. Slip along the faults produces fault gouge and damage zones [*Scholz*, 2002], which would be mechanically weaker than the surrounding rock if the fault occurred in crystalline bedrock. Alternatively, faults commonly channel groundwater [e.g., *Okubo and McEwen*, 2007], resulting in extensive mineralization that could strengthen the fault relative to the surrounding rock if the fault occurred in a weaker material such as an impact-generated regolith. Several examples of positive-relief ridges associated with small-scale fractures and faults on Mars have now been identified and interpreted as evidence of fluid-induced mineralization [*Okubo et al.*, 2007]. Potential strike-slip faults can be identified on the basis of their orientation relative to the paleoprincipal stresses, as indicated by nearby wrinkle ridges and graben. Assuming a coefficient of friction of 0.6 [*Scholz*, 2002], strike-slip faults should be oriented at roughly a 30° angle from the greatest horizontal principal stress, and thus a 60° angle from the strike of contemporaneous wrinkle ridges or a 30° angle from graben. Another diagnostic character of strike-slip faults is that they require a nearly linear surface trace to accommodate lateral motion, whereas wrinkle ridges and thrust faults tend to have a fairly sinuous trace. Strike-slip faulting also results in asymmetric vertical deformation of the surface, with the leading quadrants of the fault exhibiting uplift and the trailing quadrants subsidence [*Okubo and Schultz*, 2006; *ten Brink et al.*, 1996]. Finally, lateral offsets, where observed, can be compared with the predicted offset for that fault length using the displacement to length ratio [*Scholz*, 2002; *Schultz et al.*, 2004b].

[12] In this study, we emphasize the tectonic styles surrounding Tharsis, as those on the rise are likely complicated by the presence of a detached crustal cap [*Tanaka et al.*, 1991], an early history of intrusive uplift [*Phillips et al.*, 1990], or the effects of Valles Marineris tectonism on the regional stress field. In addition, the thin-shell technique applied in section 3 to investigate the Tharsis-induced

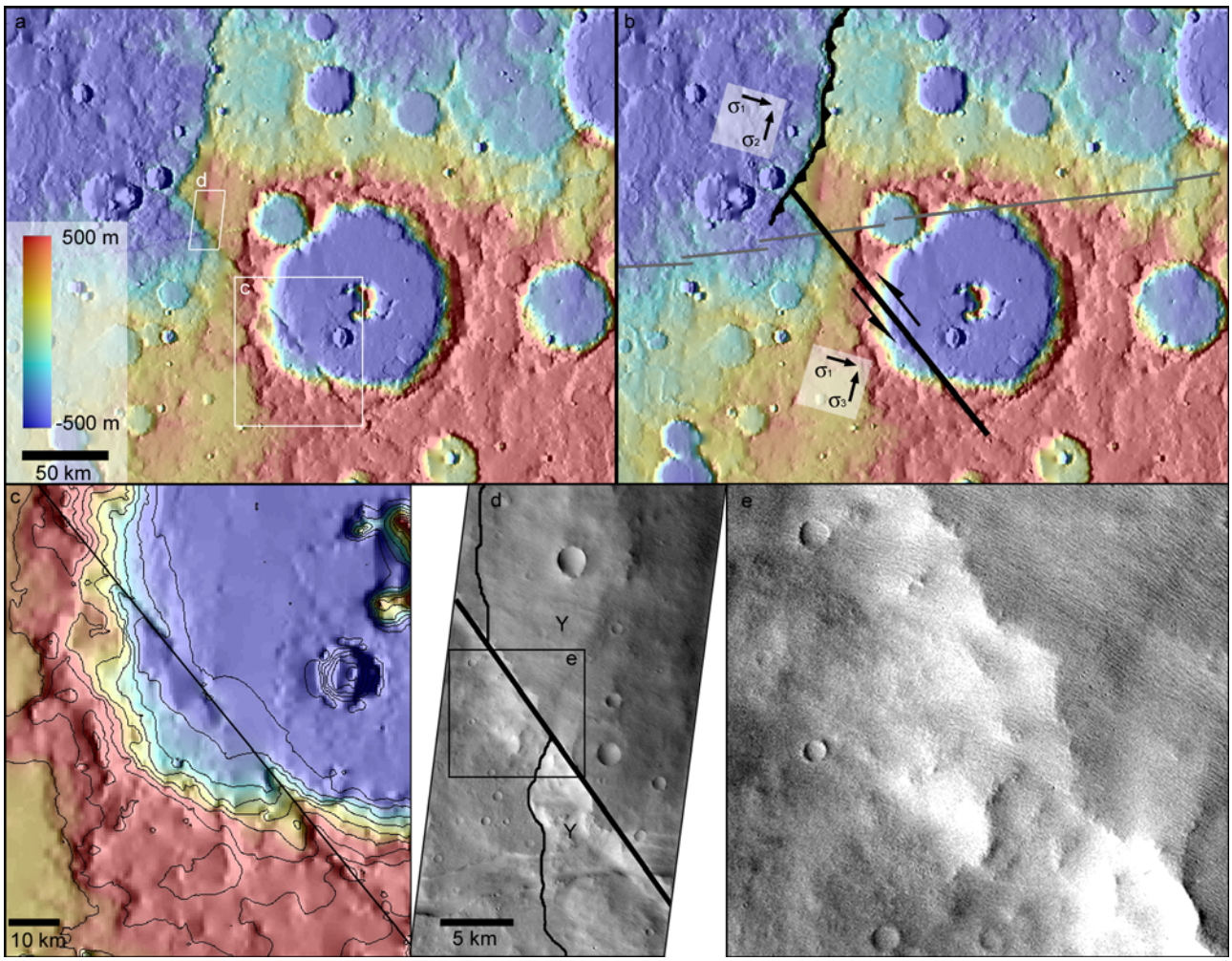

Figure 3. Candidate strike-slip fault identified as a linear scarp in MOLA topography (a) with tectonic interpretation showing sense of slip inferred from orientation of fault relative to the Tharsis-generated stress field and the location of the nearby graben (gray) and wrinkle ridge (b). Context boxes for Figures 3c–3e are shown in Figure 3a. MOLA contour map showing displacement of the southeast intersection of the fault with the crater rim; (c) contour interval 200 m. THEMIS visible image V16981003 showing offset in a friable unit being eroded into yardangs; (d, e) eroded unit labeled "Y".

stresses is valid only for the stresses within the shell itself, which is buried deep beneath the Tharsis load. We do not consider the origin of a set of strike-slip faults observed in the Coprates region south of Valles Marineris [*Schultz*, 1989; *Artita and Schultz*, 2005], since the stresses in this region would have been strongly influenced by Valles Marineris tectonism and cannot be reliably predicted by the model. In the next sections, we use the criteria above in the identification of strike-slip faults in the region west of Tharsis.

2.3. Southwest (Memnonia) Strike-Slip Faults

[13] We have used MOLA topography and shaded relief to map 19 potential strike-slip faults in the Memnonia region to the southwest of Tharsis on the basis of their orientation and general morphology (hereafter referred to as the Memnonia strike-slip faults; Figure 2). There are two populations of graben in the region, associated with tectonic stages 1 and 3 of *Anderson et al.* [2001]. Most of the potential strike-slip faults have orientations relative to the principal stress directions indicated by the stage 1 graben consistent with formation during stage 1 tectonism in the Noachian. As a result of their age and degraded state, many of the faults of this population do not present any obvious manifestation of strike-slip faulting besides their linearity and orientation. Most of the faults are manifest as positive relief features, suggesting differential erosion of the surrounding terrain since the most recent tectonic activity. However, a few of the faults exhibit clear evidence of the sense and magnitude of their displacements, thereby lending credence to the strike-slip interpretation of the rest of the population.

[14] The clearest example of a strike-slip fault was identified as a ~200-km-long linear scarp with positive relief (Figure 3). The fault is at nearly a 30° angle from the orientation of the nearby stage 1 graben, and crosses one of the stage 3 graben without offsetting it, suggesting formation prior to the end of stage 3 tectonism. The orientation of the fault relative to the principal stress directions suggests left lateral slip. The topography around the fault shows an

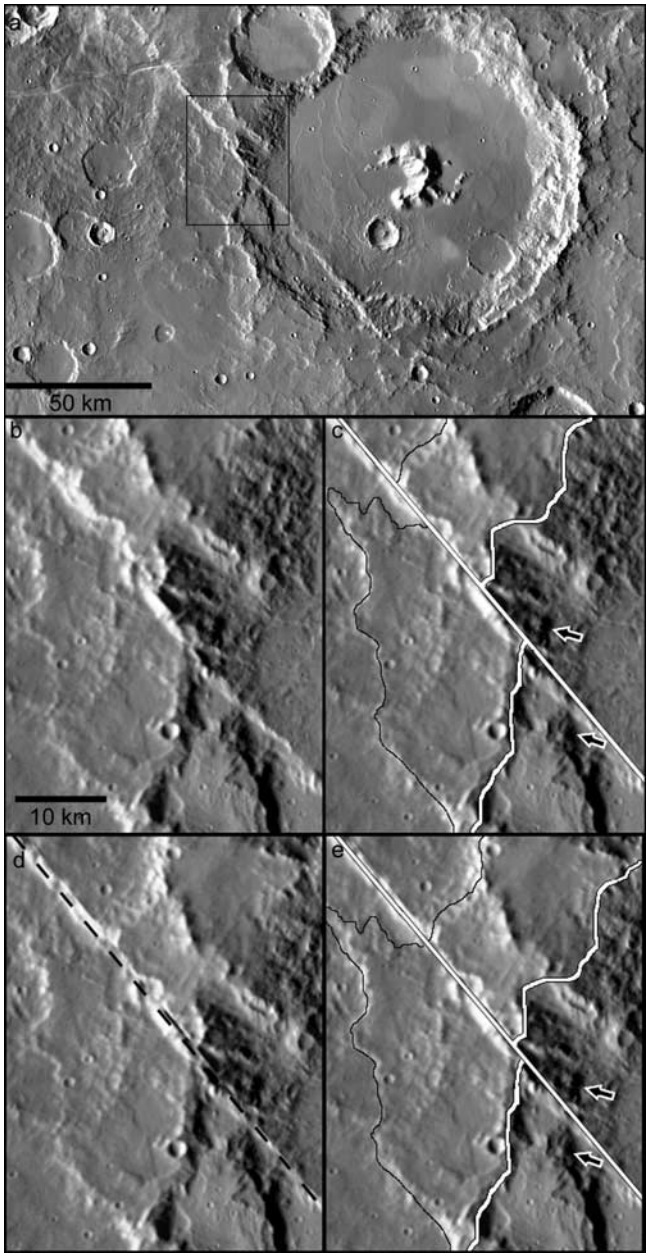

Figure 4. (a) THEMIS daytime IR image mosaic of the proposed strike-slip fault shown in Figure 3. Lower panels show (b) an enlargement of the NW intersection of the fault with the crater rim and (c) the geologic interpretation, tracing the fault and crater rim (white line), a lobate unit interpreted to be the eroded remnant of the crater ejecta (thin black line), and terraces inside the crater rim (arrows). (d, e) The reconstruction of the crater rim prior to strike-slip displacement along the fault is shown by shifting the southwest fault block ~7 km toward the northeast.

uplift of several hundred meters in the northwest leading quadrant, consistent with the inferred sense of slip. The fault intersects the rim of a large crater in two places, and appears to have postdated the formation of that crater. Contour lines in the southeast intersection of the fault with the crater rim are offset by ~5 km (Figure 3c), consistent with the inferred sense of the slip and the ~6 km displacement predicted based on the terrestrial D:L ratio, though noticeably greater than the displacement of ~1.2 km predicted by the lower D:L ratio of *Schultz et al.* [2004b].

[15] The offset in the northwest intersection of the fault with the crater rim is not as obvious in MOLA topography, partly due to the fact that the crater rim is roughly parallel to the MOLA tracks in this location, and the ~1 km spacing between tracks decreases the likelihood that this offset would be resolved. However, evidence for the displacement across the fault at the northwest intersection with the crater rim is seen in a THEMIS daytime infrared image mosaic, which reveals an offset of approximately 7 km in the main crater rim (Figure 4). We have also identified evidence for a similar offset in a terrace on the crater wall, and a unit outside the crater rim that may represent an eroded remnant of the ejecta blanket. The consistency of the offset of these features can be seen by shifting the southwest fault block by ~7 km toward the northwest, resulting in alignment of the offset boundaries. Similarly a low ridge of friable material further to the west that has been eroded into yardangs is offset by approximately 9 km, juxtaposing terrains with and without yardangs on either side of the fault (Figures 3d and 3e). However, the fault is highly degraded and the irregularity of the intersected crater rim and ridge makes the unambiguous identification of offsets difficult. While these observations are subject to alternative interpretations, the consistency of the offsets detected in multiple locations along the fault argues for the validity of this interpretation.

[16] The preservation of this fault as a ridge suggests that the fault rocks were more resistant to erosion than the host rocks, possibly due to water-induced mineralization of the fault gouge and damage zones. The width of the ridge of several 100 m to 1 km can be compared with the predicted width of the fault gouge and damage zones. Terrestrial faults exhibit a constant ratio between the width of the fault gouge zone and the total fault displacement of ~0.01, with a range of 0.001 to 0.1 [*Scholz*, 2002]. Thus the observed displacement of ~5 km would lead to predicted widths of the fault gouge zone of 5 to 500 m. Similarly, the terrestrial ratio between the width of the heavily fractured fault damage zone and the displacement of ~1 [*Scholz*, 2002] would lead to a predicted damage zone width of ~5 km. Thus the observed width of the ridge is consistent with the hypothesis that the fractures surrounding the fault channeled fluids, leading to cementation of the surrounding megaregolith and preferential resistance to erosion.

[17] The fault scarp trends at an angle of approximately 60° to the nearest wrinkle ridge, and appears to be continuous with the underlying thrust fault. As a result, the northwest end of the strike-slip fault would have been permitted some degree of vertical and horizontal movement, while the southeast end was pinned. Thus while the displacement across a fault that is pinned at both ends will reach its maximum at the midpoint of the fault, the measured displacement across this fault increases alongstrike from the southeast to the northwest. Continuity between the strike-slip and thrust faults may have contributed to the greater displacement to length ratio than predicted for Martian faults. Whether the transition from strike-slip faulting to thrust faulting occurred as a result of a

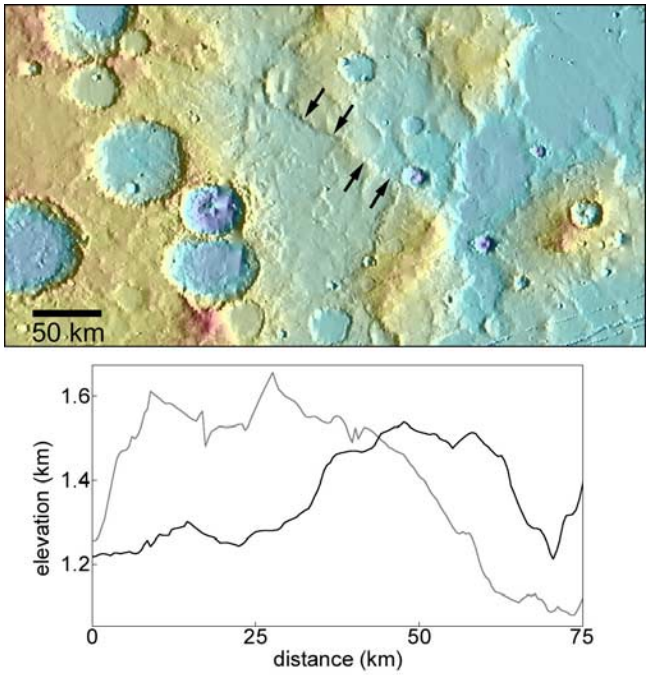

Figure 5. Asymmetric vertical throw across one of the Memnonia faults, as evidenced by opposite shading along the scarp in different quadrants in a MOLA relief map (top; see Figure 2 for context). Arrows point toward the fault from the uplifted leading quadrants. Parallel profiles along the northern (gray) and southern (black) edges of the fault reveal the asymmetric vertical uplift to be ~200 m (bottom).

temporal change in the stress field, or as a result of the strike-slip fault lengthening along-strike into a region in which thrust faulting was favored is unclear. However, the continuation of the wrinkle ridge beyond the intersection with the strike-slip fault suggests that thrust faulting persisted later than strike-slip faulting at this locale.

[18] Further south, another potential strike-slip fault with a length of 200 km exhibits a clear asymmetric vertical throw across the fault, with a leading quadrant uplift of approximately 200 to 400 m relative to the trailing quadrants (Figure 5). While no horizontal offset is detectable across this ancient fault, the observed asymmetric vertical throw is strongly diagnostic of a strike-slip faulting origin. The leading-trailing quadrant asymmetry is consistent with the predicted sense of throw for σ_1 in the Tharsis-radial direction, as would be expected due to Tharsis loading.

[19] While the other faults in the population do not display clear offsets or asymmetric vertical throw, we note that no other mechanism adequately explains the origin of such highly linear scarps at the predicted orientation relative to the inferred principal stress directions. The remainder of the Memnonia faults are identified solely on the basis of their linearity and orientation. A cursory analysis of higher resolution images did not reveal obvious evidence of offsets, though this is not surprising given the degraded state of these faults. While the identification of these features as strike-slip faults must be regarded as preliminary, alternative explanations are unsatisfactory. Although some of the faults are manifest as ridges, their morphology is wholly unlike nearby wrinkle ridges. Wrinkle ridges generally have a sinuous or crenulated surface trace, changing strike by up to 30° over short distances, whereas the proposed strike-slip faults are highly linear for distances of up to several hundred km. This linearity is required to allow for horizontal transverse displacements across the faults. A comparison of the proposed strike-slip fault in Figure 3 with the nearby wrinkle ridges demonstrates the striking difference in morphology.

[20] The orientation of the proposed faults also provides strong evidence for their strike-slip nature. While the orientations of the principal stress directions in the terrestrial lithosphere at a given locale vary greatly over geologic timescales, the stresses in the Martian lithosphere have been much more stable. Analysis of the orientations of the Noachian and Hesperian graben in this region suggests little change in the principal stress directions throughout early Mars history [*Anderson et al.*, 2001]. Furthermore, inversion of the present-day gravity and topography of Mars suggests that Tharsis is still supported largely by membrane and flexural stresses, with the principal stress directions in agreement with those deduced from the ancient fault populations [*Banerdt and Golombek*, 2000]. Thus the principal stress directions in this region have changed little in the ~4 billion year geologic record.

[21] Strike-slip faults form at acute angles to the greatest horizontal principal stress direction, with angles of ~30° for typical frictional strengths and 45° for faults with negligible friction. The orientations of the Memnonia faults relative to the σ_1 directions predicted by the stage 1 and stage 3 tectonic centers have been plotted in rose diagrams in Figure 6 (with the σ_1 direction oriented left–right). The mean fault angle is less than 45° from the stage 1 σ_1 direction, and the angle between the conjugate fault pairs is less than 90°, supporting a strike-slip origin. That the angle from σ_1 is nearly equal to 45° suggests that the frictional strength of the faults was very low. This low strength could result from high fluid pore pressures, consistent with the evidence for hydrological activity in the region at the Mangala Valles outflow channel [*Hanna and Phillips*, 2006]. The faults are greater than 45° from the σ_1 direction for the stage 3 center, arguing against a stage 3 origin. However, the San Andreas strike-slip fault is nearly parallel to adjacent thrust faults [*Mount and Suppe*, 1987], possibly due to rotation of the nearby folds [*Scholz*, 2000], suggesting that some caution must be exercised in interpreting the orientation of these proposed strike-slip faults. The dominance of the northwest-oriented faults over the northeast-oriented faults may reveal some degree of structural influence on the fault orientations.

[22] For comparison, rose diagrams have also been plotted for the stage 1 and stage 3 graben in the area, as well as a representative sampling of wrinkle ridges (relative to the stage 1 and 3 centers). The graben orientations are in agreement with the centers identified by *Anderson et al.* [2001]. The wrinkle ridge orientations fall on either side of the σ_3 direction for the stage 1 and stage 3 centers, supporting the conclusion of *Anderson et al.* [2001] that the wrinkle ridges formed over a long period of time. The orientations of the proposed strike-slip faults are clearly inconsistent with an origin as either wrinkle ridges or graben. An extensional or compressional interpretation of

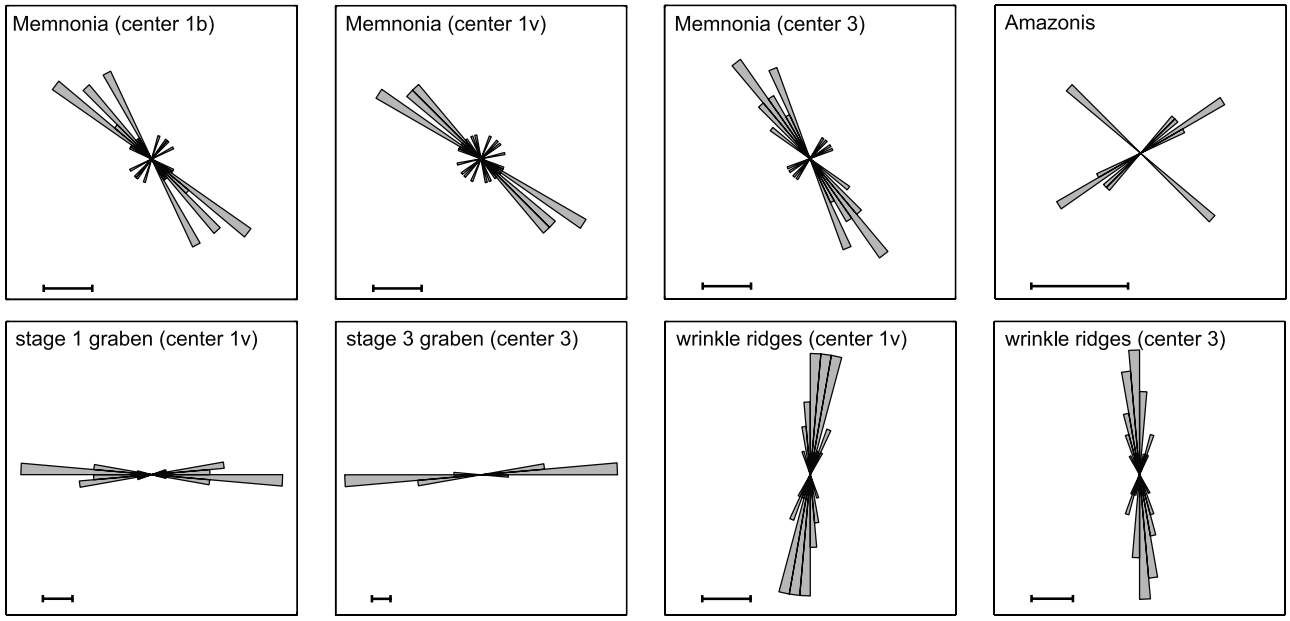

Figure 6. Rose diagrams of the proposed Memnonia strike-slip faults relative to the tectonic centers of *Anderson et al.* [2001]: center 1b, center of stage 1 tectonism from the beta analysis; center 1v, center of stage 1 tectonism from the vector analysis; center 3, center of stage 3 tectonism. In these diagrams, the σ_1 direction is oriented left–right. Also, shown is a rose diagram of the Amazonis strike-slip faults relative to the compass directions. Rose diagrams for the stages 1 and 3 graben and the wrinkle ridges are shown in the bottom. The scale bars in each panel represent a count of two faults in the rose diagrams.

the faults would require a dramatic reorientation of the principal stress directions, in conflict with all available evidence. A rose diagram of the Amazonis faults shows similar orientations, though the orientations of the principal stress directions in this region are not as well constrained due to the lack of graben and wrinkle ridges in the vicinity. Thus this rose diagram is plotted relative to the compass directions.

[23] Interestingly, despite the high density of dike-induced graben in this region, only one is seen to intersect a proposed strike-slip fault (Figures 2 and 3). This can be explained by noting that the stress release during both strike-slip faulting and graben formation would result in an increase in the magnitude of the circumferentially oriented least horizontal compressive stress and a decrease in the horizontal deviatoric stress. As the dikes propagated radially down from the Tharsis rise during stage 3 tectonism, they would have been deflected toward regions in which the circumferential stress was lower, and thus away from regions in which strike-slip faulting had led to the release of the horizontal deviatoric stress. Alternately, as a dike passed through a region in which strike-slip faults had already released the horizontal deviatoric stress, the greater normal stress perpendicular to the dike would inhibit the dike opening, leading to a more deeply buried upper dike tip and thereby preventing graben formation. Similarly, strike-slip faults would be less likely to form in regions where the formation of the dike-induced graben had increased the magnitude of the circumferential stress. In contrast, the ubiquitous thrust faulting and wrinkle ridge formation would have decreased the magnitude of the radially oriented greatest horizontal compressive stress without significantly affecting the circumferential least horizontal compressive stress, thus not affecting the formation of the radial dikes.

[24] This effect can be seen in the southernmost group of proposed strike-slip faults in the population (Figure 7). These faults appear to have been partly resurfaced by Hesperian lava flows, and are thus poorly expressed at the surface. One of the faults maintains a uniform strike for a distance of ~200 km, until approaching a graben and being deflected horizontally into a curvilinear arc and apparently transitioning into a thrust fault before terminating (Figure 7, arrow). Other smaller faults in this group are also deflected as they approach the graben, and none of the faults cross the graben. Intrusion of the dike underlying the graben likely increased the magnitude of the stress in the original σ_3 direction sufficiently to push the region immediately around the graben into the thrust-faulting regime. The stress-shadow around the dike would have been on the order of the thickness of the seismogenic brittle upper crust, and so would be expected to be several tens of kilometers [*Hanna and Phillips*, 2006]. This graben is part of the stage 3 episode of tectonism [*Anderson et al.*, 2001], suggesting continued activity of these southern strike-slip faults into the Hesperian epoch, after faulting had ceased in the Noachian faults further to the north.

[25] Based on their orientations and stratigraphic relationships, the majority of the Memnonia strike-slip faults appear to have formed primarily during stage 1 tectonism in the Noachian, with some faults showing evidence of activity persisting into stage 3 tectonism in the Hesperian. The degraded nature of the faults suggests that none of them were active in the Late Hesperian to Amazonian, after the decline in erosion rates [*Golombek et al.*, 2006]. We consider an age of Noachian to Early Hesperian as repre-

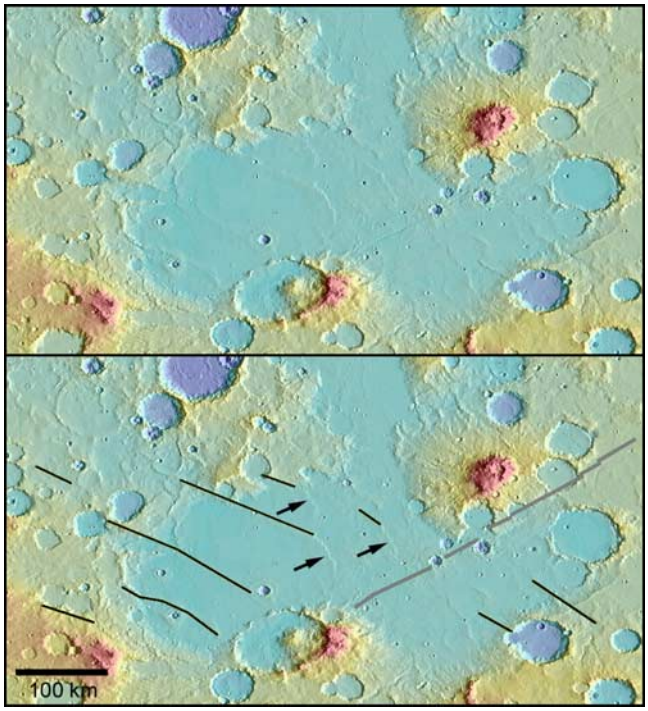

Figure 7. Parallel lineations interpreted as potential strike-slip faults (black) resurfaced by Hesperian volcanics (see Figure 2 for context). Note the deflection of the candidate strike-slip faults (arrows) away from the trace of a preexisting dike induced graben (gray).

sentative of the population as a whole, though it is difficult to place firm constraints on the onset of the strike-slip faulting. However, it is clear that tectonism in this region became dominantly compressional during the Hesperian, as evidenced by the large number of superimposed Hesperian-aged wrinkle ridges. That the strike-slip faults predate the wrinkle ridges is made clear by both their heavily degraded nature, with most faults manifesting as differentially eroded high-relief features, and their stratigraphic relationship relative to the graben and lava flows. We will consider the implication of the ages and locations of these faults for the geodynamic evolution of Mars in section 3.

2.4. Northwest (Amazonis) Strike-Slip Faults

[26] A number of strike-slip faults were recently documented in Amazonis Planitia to the northwest of Tharsis (hereafter referred to as the Amazonis strike-slip faults; Figure 8) [*Okubo and Schultz*, 2006; *Tanaka et al.*, 2003]. Detailed analysis revealed asymmetric vertical throws on all of the faults in this region, clearly demonstrating their strike-slip nature [*Okubo and Schultz*, 2006]. That study suggested an Early Amazonian age for these faults, though we reexamine their timing below. Based on a consideration of the principal stress directions inferred from the fault orientations and the apparent crosscutting of a thrust fault by a strike-slip fault, these faults were interpreted as resulting from a decrease in the magnitude of the horizontal principal stresses as a result of an increase in the degree of isostatic support of the Tharsis rise [*Okubo and Schultz*, 2006].

[27] The original identification and characterization of the fault scarps made use of MOLA topography and shaded relief maps, which clearly showed the fault scarps crossing Early Amazonian lava flows (Figure 8). The faults have lengths ranging from 200 to 450 km, suggesting horizontal displacements of between 1.2 and 2.7 km for displacement to length ratios of 6×10^{-3} [*Schultz et al.*, 2004b], or between 6.0 and 13.5 km for D:L ratios of 3×10^{-2} [*Hauber et al.*, 2007; *Scholz*, 2002]. However, there are no instances of measurable horizontal offsets across any of the strike-slip faults in THEMIS visible and infrared images down to a resolution of ~10 meters per pixel, despite the relatively pristine nature of the Amazonian-aged surface materials (Figure 9). In some instances, the faults do not even break the surface and the primary textures of the lava flows are uninterrupted across the fault (Figure 9a). In this case, the lack of fault break occurs in one of the youngest lava flows in the region (unit Als1-Young of *Okubo and Schultz* [2006]), dated as Middle Amazonian [*Tanaka et al.*, 2003], suggesting that strike-slip faulting had ceased by this time.

[28] In other images, the faults are seen to break the surface in a series of discontinuous en echelon cracks, which would not permit continuous along-strike displacement at the surface (Figures 9b and 9c). This morphology is similar to that seen in a case of a buried strike-slip fault partially rupturing an overlying younger lava flow in Iceland, resulting in a discontinuous surface rupture [*Einarsson*

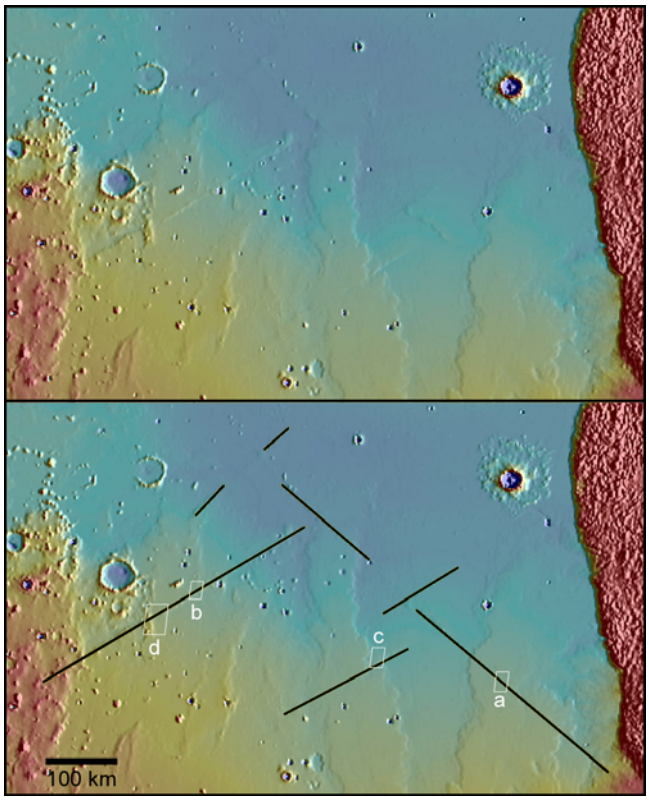

Figure 8. MOLA map of strike-slip faults (black lines) in Amazonis Planitia, as mapped by *Tanaka et al.* [2003] and *Okubo and Schultz* [2006]. Context boxes for Figures 9a–9d are shown in the bottom.

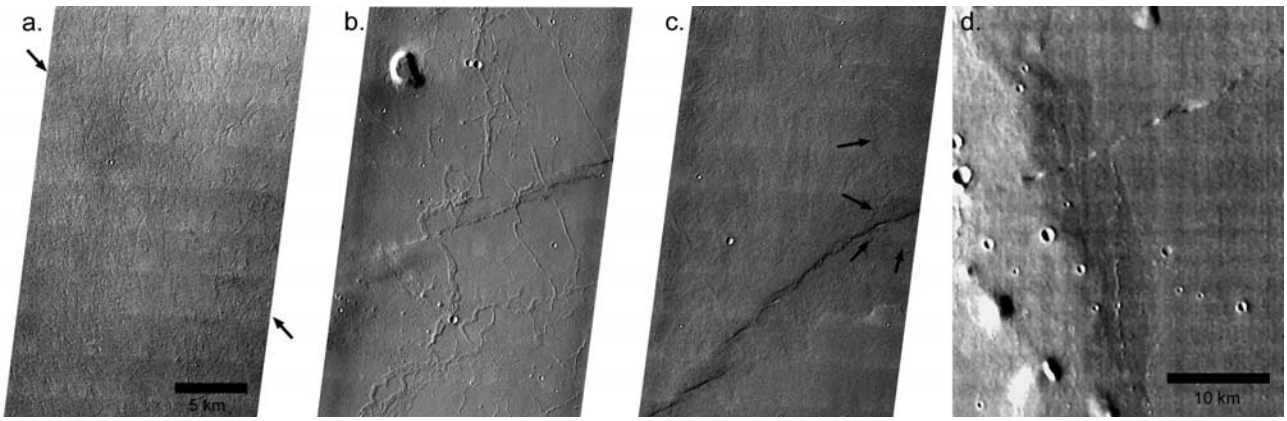

Figure 9. THEMIS visible and infrared images showing details of the Amazonis strike-slip faults: (a) an Amazonian lava flow in which the fault can be traced (arrows) despite a lack of obvious surface rupture and the continuity of the surface texture of the flow across the fault (THEMIS image V12350009); (b) fine ridges on a Late Hesperian–Early Amazonian lava flow which are not displaced across the faults, note also the discontinuous en echelon pattern of the fault (THEMIS image V10990006); (c) Amazonian-aged lava flows crossed by a discontinuous en echelon fault, with no obvious displacement of flow fronts (arrows) or surface features (THEMIS image V12113006); (d) a lobate ridge cut by a strike-slip fault showing no evidence of horizontal offset of either the ridge or the embaying lava flow (THEMIS infrared image I18066021).

and Eiriksson, 1982]. Laboratory studies of basement-controlled faulting, in which slip is induced on a preexisting fault underlying an unruptured surface layer, also demonstrate development of discontinuous Riedel shears as seen in Figures 9b and 9c [*Naylor et al.*, 1986]. These reactivated faults are seen in units AHl and Als1-Old by *Tanaka et al.* [2003] and *Okubo and Schultz* [2006], dating to the Late Hesperian and Early Amazonian. Thus while the faults may be fully developed at depth, it seems that there has been only minor horizontal displacement across the faults at the surface since the emplacement of the Early Amazonian lava flows, and none since the Middle Amazonian, with the bulk of strike-slip activity predating this resurfacing.

[29] The observed vertical throw [*Okubo and Schultz*, 2006] may be explained as a result of the emplacement of thin lava flows over a preexisting fault scarp, preserving some topographic expression of the scarp. Support for this possibility comes from recent images of Athabasca Valles suggesting that this channel has been extensively resurfaced by thin lava flows, while still preserving much of the small-scale topography of the channel floor [*Jaeger et al.*, 2007]. Alternatively, the observed throw may be a result of either fault rupture or aseismic creep occurring at depth, which could have produced minimal horizontal displacement at the surface while still generating vertical throw. However, supporting evidence or a suitable analog for such a scenario is lacking. In any event, the consistency of the vertical throw along the full trace of the faults suggests that the fault at depth is fully developed and continuous, and thus the typical displacement–length relationships for mature faults should apply. Thus we conclude that the activity on these strike-slip faults largely preceded the emplacement of the Amazonian lava flows, with only minor activity in the Early Amazonian. We cannot, however, constrain the onset of strike-slip faulting in this region, other than to say that the majority of the fault activity was likely Hesperian or older.

[30] The Amazonis strike-slip faults overlap with the wrinkle ridges to the west, and a transition from thrust faulting to strike-slip faulting was proposed based on the intersection of one strike-slip fault with a ridge [*Okubo and Schultz*, 2006]. However, establishing the relative ages of the faults with certainty requires the use of crosscutting relationships, and the observation of an offset (or lack thereof) of the ridge across the strike-slip fault. There is only one instance of a strike-slip fault crossing a ridge, and THEMIS daytime infrared images reveal that there is no measurable offset across the strike-slip fault of either the ridge or the adjacent margin of a lobate unit (Figure 9d). The ~450 km length of this fault would suggest a displacement of 2.7 to 13.5 km. For comparison, displacements of 5 to 10 km were readily apparent for one of the older and more degraded Memnonia strike-slip faults discussed above. The observed surface break of this strike-slip fault is likely a result of more recent activation with little horizontal displacement, as discussed above. This lack of displacement of the ridge suggests that at this particular locale, the majority of the strike-slip faulting preceded the thrust faulting. This is in agreement with the stratigraphic relationships, which suggest that wrinkle ridge formation in this locale occurred between the emplacement of the older and younger Als1 lava flows [*Tanaka et al.*, 2003], while the majority of the strike-slip faulting predated all of the Amazonian-aged flows in the region, and strike-slip fault reactivation had ceased altogether by the emplacement of the younger Als1 flow. Similarly, in another area of the planet, *Schultz* [1989] concluded that strike-slip faulting in the Coprates region either preceded or was contemporaneous with wrinkle ridge formation there.

[31] An alternative possibility is that loading by Amazonian lava flows could have increased the vertical stress relative to the horizontal stresses, triggering a change from thrust to strike-slip faulting and causing the reactivation of the

Amazonis faults. While it is impossible to rule this scenario out, we note that the lack of wrinkle ridges throughout most of the region of the Amazonis strike-slip faults does not support this scenario. Furthermore, the thin lava flows required to preserve the asymmetric vertical throw (about tens of meters) would add little to the overburden ($\sim$0.1 MPa). Thus the region would be required to have been on the threshold between strike-slip and thrust faulting at the time the flows were emplaced in this scenario. In the following section, we consider the effect of contractional stresses of tens to hundreds of MPa on the predicted style of faulting, and so the effects of this added overburden are negligible in comparison. We favor the interpretation that the region underwent a transition from strike-slip to thrust faulting sometime in the Late Amazonian, with the observed fault breaks representing the tail end of strike-slip activity.

2.5. Summary

[32] The two populations of strike-slip faults to the west of Tharsis provide us with a history of strike-slip faulting spanning roughly two billion years. Strike-slip faulting began southwest of Tharsis during stage 1 tectonism in the Noachian. Unlike the nearby graben, which formed in discrete dike-injection events, the strike-slip faults would likely have developed through intermittent tectonic activity over a long period of time, as is observed on the Earth. The majority of the tectonic activity likely occurred during the Noachian, as evidenced by the eroded state of most of the faults, their orientations with respect to the stage 1 graben, and superposition relationships relative to the stage 3 graben. Some strike-slip activity continuing into the Hesperian is suggested by the southernmost cluster of faults, which appear to be deflected in the vicinity of a stage 3 graben.

[33] In contrast, the previously identified faults northwest of Tharsis appear to have experienced activity more recently in Mars history. While the onset of faulting is poorly constrained, the majority of the tectonic activity appears to have preceded emplacement of the Amazonian lava flows in this area. However, continued activity of the faults during the Early Amazonian is indicated by the presence of fresh fault breaks in some of the lava flow units. Thus strike-slip faulting northwest of Tharsis continued for nearly 1 billion years after the termination of faulting southwest of Tharsis in the Late Noachian to Early Hesperian. This evidence for shifting loci of strike-slip faulting provides us with a constraint on the evolving stress state of Mars.

3. Stress Modeling and Implications

3.1. Loading and Contractional Stresses: Predicted Styles of Tectonism

[34] Having documented evidence for a long history of strike-slip faulting west of Tharsis, stretching from the Noachian through the Amazonian, we now turn our attention to the predicted styles of tectonism. We first consider the stresses and tectonic styles predicted from loading alone, as done previously by *Banerdt et al.* [1992] and *Banerdt and Golombek* [2000]. The global gravity and topography [*Smith et al.*, 1999a, 1999b] are inverted under the assumption of crustal-compensated flexure, solving for the surface and subsurface loads and resulting stress patterns using the analytic spherical harmonic model by *Banerdt* [1986], based on the thin-shell theory by *Vlasov* [1964]. We use the spherical harmonic gravity model JGM95I01 (G. L. Tyler et al., JGM95I01.SHA, in MGS RST Science Data Products, USA_NASA_JPL_ MORS_1024, edited by R.A. Simpson, Data set MGS-MRSS-5-SDP-V1.0, 2004, NASA Planetary Data System, available at http://pds-geosciences.wustl.edu/missions/mgs/rsdata.html).

[35] The Tharsis-induced stresses are sensitive to the choice of lithosphere parameters in the inversion of the gravity and topography, particularly the lithosphere thickness at the time of Tharsis loading in the Noachian, which is also the most poorly constrained parameter. An admittance analysis of Mars [*McGovern et al.*, 2002, 2004] calculated a lithosphere thickness of less than 15 km in the Noachian, increasing to $\sim$15–60 km in the Hesperian, and to <200 km in the Amazonian. The lack of significant relaxation of the Hellas basin has been used to calculate a lithosphere thickness of $\sim$30 km at the time of that basin forming impact [*Smith et al.*, 1999b]. Models of the thermal evolution of Mars can be used to calculate the elastic lithosphere thickness, with values at the end of the Noachian ranging from 15–20 km [*Schubert and Spohn*, 1990; *Grott and Breuer*, 2008] to 50 km [*Hauck and Phillips*, 2002]. An independent constraint on the thickness of the lithosphere comes from the inferred thickness of the magnetized layer responsible for the Martian magnetic anomalies, which likely formed sometime during the Early Noachian based on the demagnetization observed in the large impact basins [*Mohit and Arkani-Hamed*, 2004]. The similarity between the magnetic blocking temperature (580°C for magnetite) and the elastic blocking temperature ($\sim$600°C [*McNutt*, 1984]), suggests that the maximum depth of magnetization of 35 km [*Nimmo and Gilmore*, 2001] corresponds roughly with the lithosphere thickness at that time.

[36] Alternatively, models of the loading of the lithosphere by the Tharsis rise using a forward approach find that the observed global-scale gravity anomalies induced by Tharsis formation are most consistent with a lithosphere thickness of $\sim$100 km [*Phillips et al.*, 2001; *Andrews-Hanna*, unpublished work]. A possible explanation for this discrepancy in lithosphere thickness estimates is that the short-wavelength, low amplitude deformation can be supported entirely by the stresses within the elastic upper crust, which is separated from the mantle lithosphere by a ductile lower crust. In contrast, the long-wavelength, large amplitude deformation induced by Tharsis may involve support from both the mantle and crustal lithosphere. We also note that the thin lithosphere deduced beneath the Tharsis Montes may reflect local thermal anomalies associated with the volcanism, whereas the long-wavelength component of the Tharsis rise requires global support and would thus extend far beyond the influence of any Tharsis-related thermal effects. It will later be shown that the tectonic evolution is most consistent with a lithosphere thickness (T_e) of 100 km, so we make this our nominal model, assuming also a Young's modulus (E) of 100 GPa, and Poisson's ratio (ν) of 0.25. We also consider lithosphere thicknesses ranging from 10 to 200 km, Young's moduli of 50 and 200 GPa, and a Poisson's ratio of 0.5. All models assume a mean crustal thickness of 50 km [*Neumann et al.*, 2004; *Wieczorek and Zuber*, 2004; *Zuber et al.*, 2000].

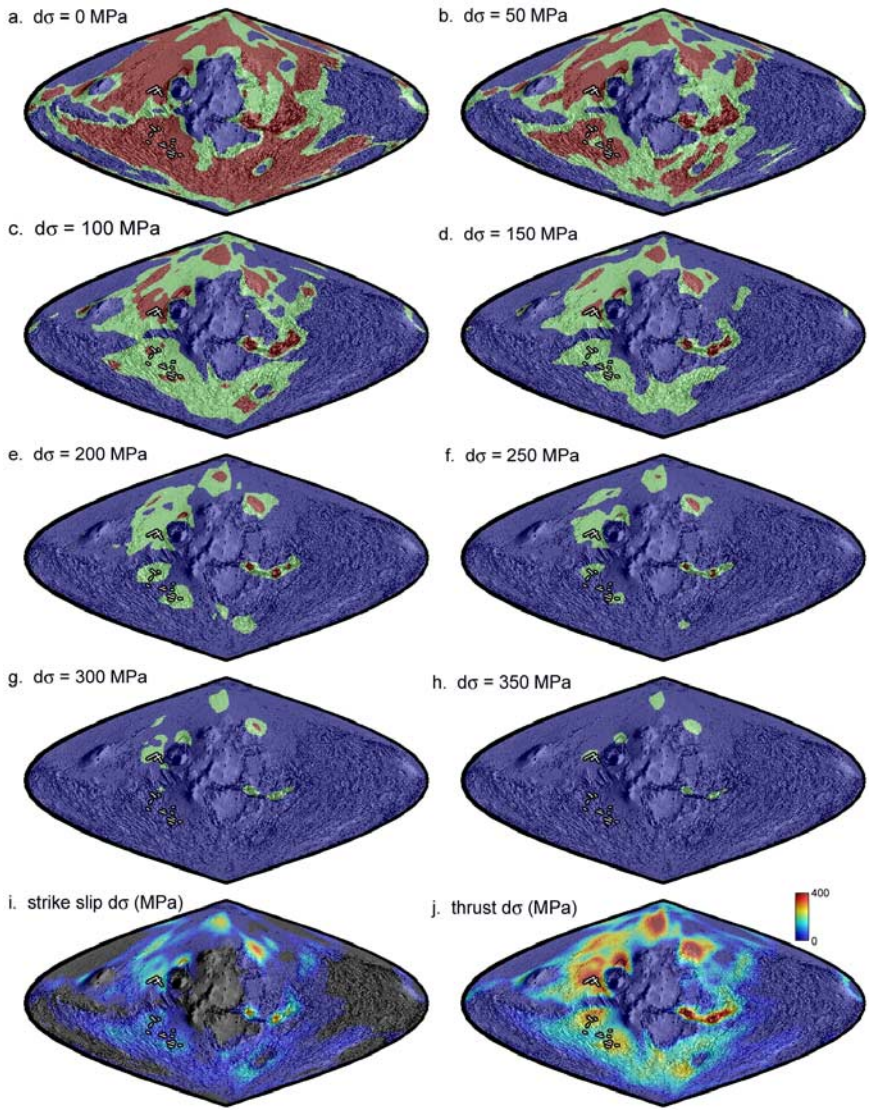

Figure 10. Predicted style of faulting as a function of the magnitude of the added contractional stress (a–h), showing zones of compressional (blue), strike-slip (green), and extensional (red) faulting. Model assumes a lithosphere thickness of 100 km, Young's modulus of 100 GPa, and Poisson's ratio of 0.25. Strike-slip faults identified by *Okubo and Schultz* [2006] and this study traced for comparison. The figures are in sinusoidal projection centered on the Tharsis rise, overlaid with MOLA-shaded relief. Also, shown are the contractional stresses necessary to push the predicted style of tectonism to strike-slip (i) and thrust (j) faulting. Regions predicted to experience thrust faulting in the absence of additional contractional stresses show up as black in Figure 10i.

[37] The membrane-flexural stresses in the lithosphere from the thin-shell model are used to calculate the predicted mode of tectonism, with compressional, strike-slip, and extensional faulting predicted when σ_3, σ_2, and σ_1 are vertical, respectively. Thus in this section we simply consider the preferred mode of tectonism if failure does occur. Section 3.2 will then consider whether the deviatoric stresses exceed the threshold stresses required to initiate faulting [*Schultz and Zuber*, 1994]. The tectonic predictions resulting from Tharsis loading for the nominal model with a 100-km-thick lithosphere are shown in Figure 10a. As found in previous studies, Tharsis is surrounded by a large region of predicted radial extensional tectonism, in agreement with the observed distribution of graben. Strike-slip faulting is predicted to be largely limited to a narrow belt surrounding Tharsis. Notably, none of the observed strike-slip faults fall entirely within the predicted region.

[38] The simple loading model neglected the superimposed contractional stress field, which would have modified the predicted styles of tectonism. The tectonic history discussed in section 2.1 suggests that the bulk of the loading stresses were emplaced during the Noachian, with only modest and localized loading during the Hesperian and Amazonian. The rate of global contraction, on the other hand, appears to have reached its peak during the Hesperian, but likely continued at a more modest rate throughout Mars

history. Thus the majority of the loading-induced stresses preceded the majority of the contractional stresses. The wide distribution of Hesperian wrinkle ridges both around Tharsis and throughout the northern lowlands [*Head et al.*, 2002] suggests that the stress state across much of the planet had become compressional by the end of the Hesperian. The evolving balance between these two stress fields over time would have driven a commensurate evolution in tectonic styles.

[39] We investigate the effects of such an evolving stress state by adding uniform horizontal compressive stresses of successively increasing magnitude to the loading-induced stresses, until a globally compressional stress state is achieved. The resulting tectonic predictions for the nominal model with a lithosphere thickness of 100 km are shown in Figures 10b–10h. The predicted style of tectonism for a given combination of loading and contractional stresses differs greatly from that based on the loading stresses alone. The increase in the horizontal compressive stress changes the balance between the principal stress directions, pushing the faulting prediction for regions originally predicted to have experienced normal faulting (σ_2 and σ_3 horizontal), into first the strike-slip faulting (σ_1 and σ_3 horizontal) and finally the thrust faulting regime (σ_1 and σ_2 horizontal). After the addition of a horizontal compressive stress of $\sim$400 MPa, nearly the entire lithosphere has become compressional in the nominal model. As the balance between the stress fields changed, roughly half of the planet would have passed through the strike-slip faulting regime, with strike-slip faulting predicted in some regions long after much of the rest of the planet had become compressional (Figures 10e and 10f). The total contractional stress required to change the predicted style of tectonism in different regions of the planet into first strike-slip and then thrust faulting is shown in Figures 10i and 10j. The two observed populations of strike-slip faults are now seen to fall within the zone of predicted strike-slip faulting for different ranges of applied contractional stresses. In section 3.3, we will consider the implications of the observed populations of faults for the stress and strain history of Mars, as well as the effects of different parameter choices.

3.2. Loading and Contractional Stresses: Critical Stresses

[40] The above discussion considered only the style of faulting predicted by the principal stress directions resulting from the combined loading and contractional stresses. The horizontal orientation of the least and greatest principal stresses is a necessary, but not sufficient, condition for strike-slip faulting. It is further required that the magnitude of the horizontal deviatoric stresses must exceed the critical stress required to initiate faulting. *Schultz and Zuber* [1994] found that the stresses generated during the growth of large planetary loads predict tensile jointing rather than strike-slip faulting at the surface if the magnitude of the negative least horizontal compressive stress exceeds the tensile strength of the crust. The formation of strike-slip faults would then require that the remaining horizontal deviatoric stresses exceed the critical stress required for faulting after the minimum horizontal principal stress has been reduced below the tensile strength of the crust. At greater depths, the added lithostatic pressure will increase the magnitude of all three principal stress vectors, thus reducing the likelihood of tensile failure. It has also been noted that the accumulation of crater ejecta on the surface can change the relative magnitudes of the principle stresses at depth [*Golombek*, 1985], though we do not consider this effect here.

[41] It was demonstrated in the previous section that much of the Martian crust passes through the strike-slip faulting regime for some combination of loading and contractional stresses. We now test whether the horizontal deviatoric stresses in the regions of predicted strike-slip faulting are sufficient to cause faults to form. We take the predicted loading-induced stresses and impose the limitation that the magnitude of any tensile principal stresses at the time of loading cannot exceed the tensile strength of the crust. Then, for each location across the planet in which strike-slip faulting is possible, we add the minimum contractional stress necessary to push the crust into the strike-slip faulting regime at that point. The resulting horizontal deviatoric stresses are compared with the critical stresses required to form strike-slip faults using the Hoek-Brown criterion [*Hoek and Brown*, 1980]:

$$(\sigma_1 - \sigma_3)_{crit} = \sqrt{m \cdot \sigma_c \sigma_3 - s \cdot \sigma_c^2} \quad (1)$$

where $(\sigma_1 - \sigma_3)_{crit}$ is the critical deviatoric stress required to drive faulting, σ_c is the compressive strength of basalt, taken to be 262 MPa, and m and s are empirical constants, taken to be 6.3 and 0.021, respectively [*Schultz and Zuber*, 1994]. Thus this approach tests whether faults will form at a given location at the point at which the added contractional stresses are just sufficient to push the crust into the theoretical strike-slip faulting regime as indicated by the orientation of the principal stress vectors. The results are sensitive to both the elastic properties of the lithosphere assumed in calculating the loading stresses and the depth within the crust, as the added lithostatic pressure will both inhibit tensile failure and change the magnitude of the critical deviatoric stress in equation (1). We here consider depths of 0 and 10 km, and lithosphere thicknesses ranging from 25 to 200 km (Figure 11). Predictions for a lithosphere thickness of 10 km are nearly indistinguishable from the 25 km case, and so are not shown.

[42] At the surface, the required conditions to form strike-slip faults are rarely met. Over the portions of the surface predicted to experience extensional faulting after loading of the lithosphere (Figure 10a), both horizontal principal stresses are strongly extensional at the surface, predicting orthogonal sets of tensile joints. As a result, both horizontal principal stresses are limited to the tensile strength of the crust, and the horizontal deviatoric stress will go to zero, preventing later strike-slip faulting. In regions predicted to experience strike-slip faulting by the simple loading model, the minimum horizontal compressive stress will be limited by the tensile strength of the crust, but the maximum horizontal compressive stress will be unaffected. The horizontal deviatoric stress is thus reduced, but still exceeds the critical stress for fault development in some cases. However, the regions in which strike-slip failure is predicted to occur at the surface do not overlap with the observed faults (Figures 11a, 11c, 11e, 11g, and 11i).

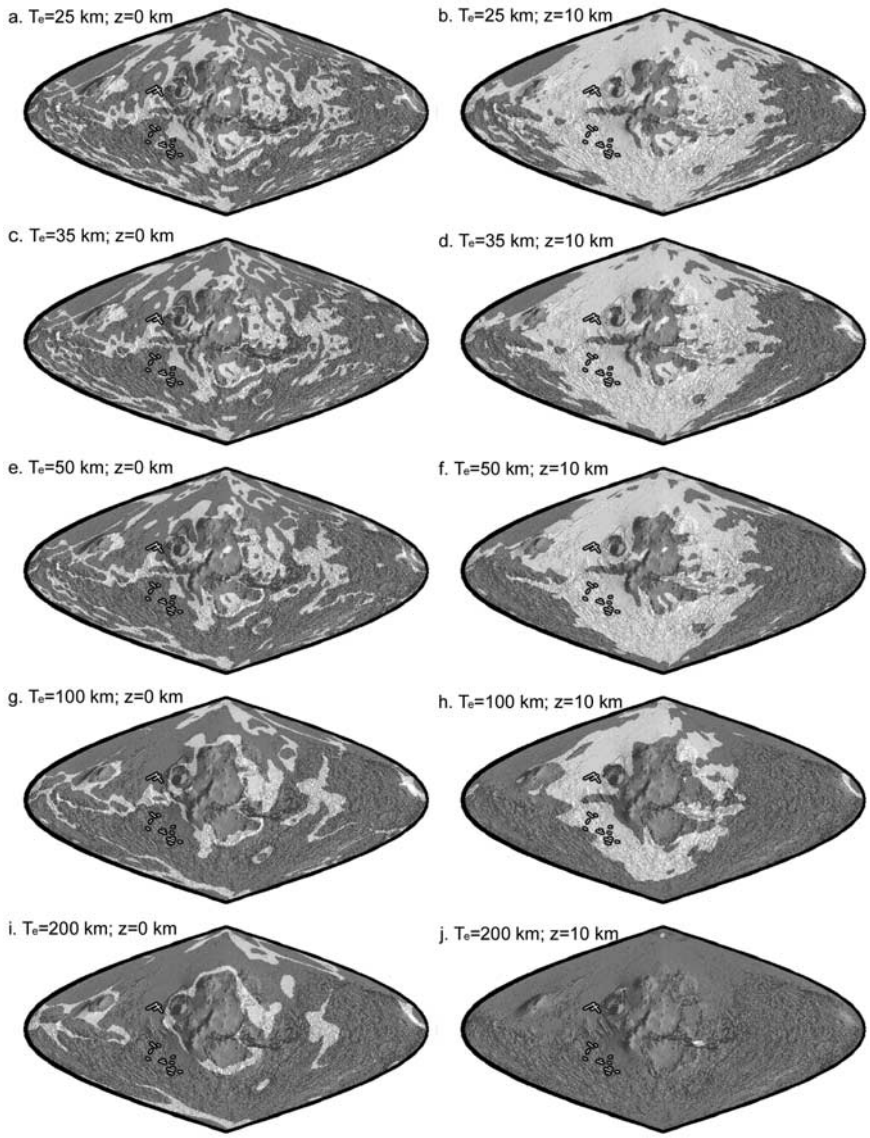

Figure 11. Regions of the planet in which the horizontal deviatoric stress exceeds the critical stress required to initiate strike-slip faulting at depths of 0 km (left) and 10 km (right) for lithosphere thicknesses ranging from 25 to 200 km (light shades denote stresses in excess of critical). Principal stress magnitudes are limited by the tensile strength of basalt, and the critical deviatoric stress required to drive faulting is evaluated after the addition of the minimum contractional stress necessary to push each location into the strike-slip faulting regime, as discussed in the text. The figures are in sinusoidal projection centered on the Tharsis rise, overlaid with MOLA-shaded relief.

[43] The bulk of the seismogenic elastic upper crust lies below the surface, where the lithostatic pressure inhibits tensile failure and jointing. Faults that develop at depth will propagate up to the surface, and the mean deviatoric stress acting on the faults can be substantial even if that at the surface is small. At a depth of 10 km, a lithostatic pressure of approximately 100 MPa is added to the principal stresses. For lithosphere thicknesses between 25 and 50 km, the remaining horizontal deviatoric stresses after tensile failure is accounted for are sufficient to drive strike-slip faulting in any region in which the orientation of the principal stress directions for a given combination of contractional and loading stresses will allow it (Figures 11b, 11d, and 11f). Thus for these thinner lithospheres, strike-slip faulting would be expected to be much more widespread than is actually observed. For a lithosphere thickness of 100 km, the horizontal deviatoric stresses are smaller, and do not exceed the critical stress in many areas. As a result, strike-slip faults would be expected to form over a more limited area of the planet, which coincides roughly with the distribution of the observed faults (Figure 11h). A somewhat greater depth or thicker lithosphere would further limit the region of predicted strike-slip failure. When the lithosphere thickness is increased to 200 km, the horizontal deviatoric stresses are no longer sufficient to initiate strike-slip faulting over most of the planet, including the locations of the observed faults (Figure 11j). Thus the observed loci of strike-slip faulting, and the lack of observed faults

Table 1. Summary of Stress Requirements for Strike-Slip Faulting at the Memnonia and Amazonis Faults

T_e, km	E, GPa	ν	$\sigma_{M,I}$[a], MPa	$\sigma_{M,f}$[b], MPa	$\sigma_{A,f}$[c], MPa	$\varepsilon_{M,I}$[d]	$\varepsilon_{M,f}$[e]	$\varepsilon_{A,f}$[f]
100	100	0.25	90	240	340	6.8×10^{-4}	1.8×10^{-3}	2.6×10^{-3}
10	100	0.25	0	2800	3600	0	2.1×10^{-2}	2.7×10^{-2}
25	100	0.25	200	1000	1300	1.5×10^{-3}	7.5×10^{-3}	9.8×10^{-3}
35	100	0.25	200	700	950	1.5×10^{-3}	5.3×10^{-3}	7.1×10^{-3}
50	100	0.25	150	500	700	1.1×10^{-3}	3.8×10^{-3}	5.3×10^{-3}
200	100	0.25	55	120	130	4.1×10^{-4}	9.0×10^{-4}	9.8×10^{-4}
100	200	0.25	50	280	390	1.9×10^{-4}	1.1×10^{-3}	1.5×10^{-3}
100	50	0.25	130	210	290	2.0×10^{-3}	3.2×10^{-3}	4.4×10^{-3}
100	100	0.5	90	270	380	4.5×10^{-4}	1.4×10^{-3}	1.9×10^{-3}

[a]Contractional stress at the onset of strike-slip faulting for the Memnonia faults.
[b]Contractional stress at the termination of strike-slip faulting for the Memnonia faults.
[c]Contractional stress at the termination of strike-slip faulting for the Amazonis faults.
[d]Contractional strain at the onset of strike-slip faulting for the Memnonia faults.
[e]Contractional strain at the termination of strike-slip faulting for the Memnonia faults.
[f]Contractional strain at the termination of strike-slip faulting for the Amazonis faults.

elsewhere, are most consistent with a lithosphere thickness at the time of Tharsis formation of ~100 km. However, the presence of competing sources of stress or factors such as different depths of faulting, vertical strength stratification, or preexisting structural controls on faulting could allow other values.

3.3 Inferred Stress and Strain History

[44] Comparison of the locations and ages of the Memnonia and Amazonis strike-slip faults with the model results provides us with snapshots of the global stress field at two distinct times in Mars history. Qualitatively, the progression of strike-slip faulting locales from both the regions southwest and possibly northwest of Tharsis during the Noachian to Early Hesperian, to only the region northwest of Tharsis during the Late Hesperian to Early Amazonian is consistent with the growth of global contractional stresses relative to the loading stresses during this time. Furthermore, the general lack of wrinkle ridges surrounding the Amazonis strike-slip faults suggests that there was little accumulation of contractional stresses after this time.

[45] If we assume that the vast majority of the loading stresses were in place by the end of the Noachian [*Banerdt and Golombek*, 2000; *Phillips et al.*, 2001], we can make a quantitative estimate of the accumulated global contractional stress and strain at the time of formation of the two populations of strike-slip faults. We first find the range of contractional stresses over which at least half of the faults in the Memnonia group are active, assuming a formation age of Noachian to Early Hesperian. We have no way of constraining the onset of tectonism for the Amazonis strike-slip faults, and the early tectonic activity for these faults likely overlapped with the strike-slip faulting to the south. However, we use the lack of tectonic activity at the Memnonia faults and continued tectonism at the Amazonis faults during the Late Hesperian and Early Amazonian as a constraint. We find the range of contractional stresses between the predicted termination of the Memnonia strike-slip faulting and that of the Amazonis faulting, again using the stress at which half of the faults are active as a cutoff value.

[46] For the nominal model parameters with a 100-km-thick lithosphere, the older Memnonia faults require the addition of a contractional stress of between 90 and 240 MPa (Figures 10c–10e) during the Noachian to Early Hesperian, while activity confined to the younger Amazonis faults requires a contractional stress of between 240 and 340 MPa (Figures 10e–10h) by the Late Hesperian to Early Amazonian. These stresses can be converted to strains, giving values of 0.68 to 1.8×10^{-3} and 1.8 to 2.6×10^{-3}, for the older and younger faults respectively. These global contractional strains are in agreement with the inferred global strain since the Early Hesperian of tenths of a percent, based on the density of wrinkle ridges and the assumed subsurface fault geometry [*Golombek et al.*, 2001]. Local strains will be the sum of the global contraction and the Tharsis-induced strains, and thus can be greater than or less than the global value. It is also noteworthy that the southernmost cluster of faults in the Memnonia group remains active after much of the rest of this region had transitioned into the compressional regime for most parameter choices (Figure 10f), in agreement with the earlier observation that these faults appear to have remained active into the Hesperian after faulting had ceased elsewhere.

[47] If we assume different choices for the lithosphere thickness at the time of Tharsis loading, the contractional strains inferred from the strike-slip fault locations change significantly (Table 1). Increasing the lithosphere thickness to 200 km results in a decrease in the inferred strains for the southwest and northwest faults to $4.1–9.0 \times 10^{-4}$ and $9.0–9.8 \times 10^{-4}$, respectively. Decreasing the lithosphere thickness to 35 km, results in an increase in the inferred strains for the southwest and northwest faults to $1.5–5.3 \times 10^{-3}$ and $5.3–7.1 \times 10^{-3}$, respectively. For the 100-km-thick lithosphere, increasing Young's modulus to 200 GPa results in a decrease in the inferred strains to $4.1–9.0 \times 10^{-4}$ and $9.0–9.8 \times 10^{-4}$, while decreasing Young's modulus to 50 GPa increases the strains to $2.0–3.2 \times 10^{-3}$ and $3.2–4.4 \times 10^{-3}$. Increasing the assumed value of Poisson's ratio results in only a modest decrease in the inferred contractional strains. Taking rough age ranges for the Noachian to Early Hesperian and Late Hesperian to Early Amazonian of 4.5 to 3.6 Ga, and 3.6 to 1.7 Ga, respectively [*Hartmann and Neukum*, 2001], allows us to plot the total contractional strain as a function of time (Figure 12), which will be compared with predictions from models of the thermal evolution of Mars in the next section.

[48] It must be emphasized that the simple addition of a uniform horizontal compressive stress alone is not necessar-

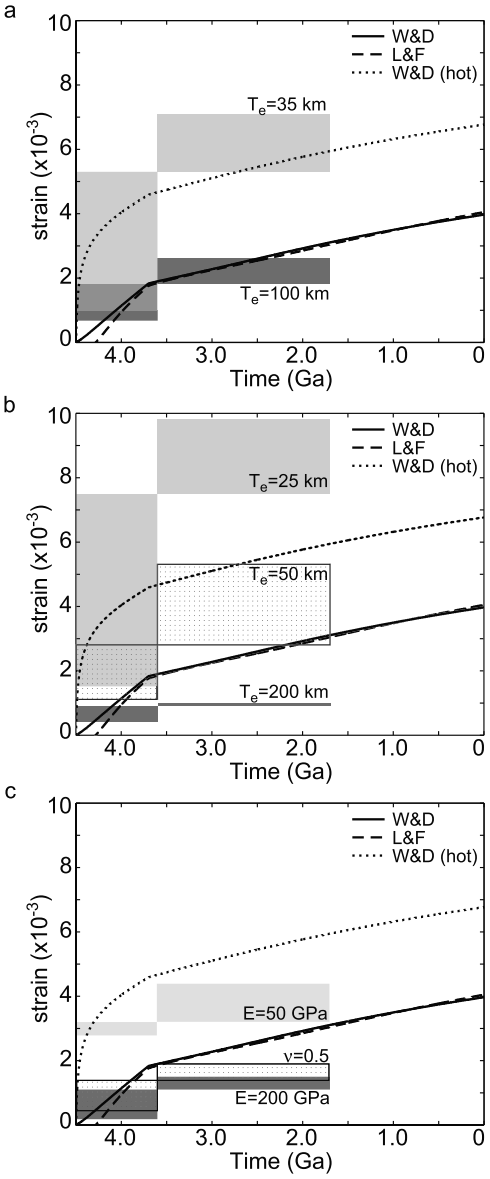

Figure 12. Total contractional strain as a function of time inferred from the locations and ages of the strike slip faults (shaded boxes), showing the effects of different choices of lithosphere thickness (a and b) or elastic parameters (c). The nominal model is represented by the 100-km-thick lithosphere in Figure 12a, all other models differ only by the choice in parameter specified. Also, shown is the predicted global contraction from the thermal evolution model of *Hauck and Phillips* [2002] for the *Wänke and Dreibus* [1994] (W&D) and *Lodders and Fegley* [1997] (L&F) compositional models, also considering the effect of an initially hot Mars (W&D (hot)). Contractional strain curves have an added component of contraction due to Tharsis formation between 4.5 and 3.7 Ga. The boxes represent strike-slip activity in Memnonia (and possibly Amazonis) in the Late Noachian to Early Hesperian and strike-slip activity only in Amazonis in the Late Hesperian to Amazonian.

ily sufficient to drive continued strike-slip faulting. For the simplistic scenario in which the deviatoric stresses are relieved instantaneously upon exceeding some threshold value required for faulting, the stress release by extensional or strike-slip faulting would occur after emplacement of the loading stresses. The critical deviatoric stress required for extensional faulting is lower than for strike-slip faulting as a result of the greater frictional strength of the faults under compression. Thus if the deviatoric stress in a given area is insufficient to trigger extensional tectonism prior to emplacement of the contractional stresses, then strike-slip faulting after the growth of the contractional stresses would not be expected. However, tectonic stress release is limited by the growth and development of faults, potentially allowing the stresses in the unfaulted lithosphere to remain above the critical values required for sliding along a preexisting fault for long periods of time. If the lithosphere is maintained at near-critical stress levels, then tectonism could also be triggered by impacts, interactions with nearby faults, or hydrological processes.

[49] Furthermore, while we have assumed that the majority of the Tharsis loading stresses were in place by the end of the Noachian, there is clear geologic evidence for some continued loading throughout the Hesperian and into the Amazonian, in the form of the late-stage veneer of volcanics on the Tharsis rise. This continued loading would not likely have changed the distribution or magnitudes of the stresses significantly, but could have been sufficient to drive continued faulting in regions that were near critical. Similarly, an early period of rapid planetary contraction likely overlapped with Tharsis loading early in Mars history, and so the loading and contractional stresses would have grown simultaneously during the Early Noachian, inhibiting early nonmagmatic extensional tectonism. The particular balance between the rates of loading and contraction would have affected the tectonic predictions in these early stages. However, the volume and extent of continued Tharsis loading appears to have been minimal since the close of the Hesperian. The predicted contractional stresses required for the initiation of tectonism at the Memnonia faults may have been affected by early contraction and late-stage Tharsis growth, but the stresses required for the termination of the Memnonia tectonism and the later termination of the Amazonis tectonism are not likely to have been affected. Since the geologic evidence for the timing of the onset of Memnonia tectonism is poorly constrained (and we have simply assumed tectonism initiating at the beginning of the Noachian), this does not affect our results or interpretations.

[50] The results above also demonstrate that wrinkle ridge formation would not have simply coincided with the peak in the rate of global contraction, as commonly assumed. Rather, wrinkle ridge formation would have commenced when the accumulated contractional stresses were sufficient to change the prediction of extensional or strike-slip faulting in the wake of Tharsis loading to one of thrust faulting, and the magnitude of the compressional stresses exceeded the critical value for failure. The wide range of contractional stresses required to invoke this transition in different parts of the planet (0 to 400 MPa for T_e = 100 km; Figure 10j) agrees with the wide range of wrinkle ridge ages. Wrinkle ridges would presumably have continued to develop as long as the contractional stresses continued to grow. This

explains the apparent discrepancy between the peak in wrinkle ridge formation in the Hesperian and the predicted peak in the contractional strain rate in the Early Noachian based on thermal models [e.g., *Hauck and Phillips*, 2002].

3.4. Theoretical Estimates of the Global Contraction

[51] The primary source of contractional strain throughout Mars history is thought to have been the steady secular cooling of the planet. Models of the thermal evolution of Mars from parameterized convection [*Hauck and Phillips*, 2002; *Schubert and Spohn*, 1990] allow us to calculate the accumulated strain as a function of time. The nominal model of *Hauck and Phillips* [2002] assumed an initially cool Mars (mantle and core temperatures of 1720 and 2000 K, respectively) with a chondritic radionuclide abundance, following *Wänke and Dreibus* [1994] (hereafter referred as the *W&D* model). They also considered a wide range of parameter space for the key parameters governing the initial state and subsequent thermal evolution. We here include two variations on the nominal model of *Hauck and Phillips* [2002]. First, we consider their results for a Mars enriched in ^{40}K, after *Lodders and Fegley* [1997] (hereafter referred to as the *L&F* model). Second, we consider their results for an initially hot Mars with mantle and core temperatures of 1973 and 2250 K, respectively (hereafter referred to as the *W&D (hot)* model). These temperatures are comparable to the near-solidus temperatures at the end of the magma ocean stage predicted by *Elkins-Tanton et al.* [2005]. The thermal models begin at 4.5 Ga, after differentiation and magma-ocean overturn would be expected to be complete [*Elkins-Tanton et al.*, 2005; *Lee and Halliday*, 1997] and an initially thin lithosphere would have begun to grow.

[52] The volumetrically averaged thermal expansivity of the Martian mantle is calculated to be 3.3×10^{-5}, using the pressure- and temperature-dependent thermal expansivity of the olivine-spinel system [*Fei*, 1995] and assuming an adiabatic mantle temperature profile. This value is greater than the average value for the Earth as a result of the lower pressures in the Martian mantle. Considering only the cooling of the planet, and neglecting phase changes in the mantle and core, we can then calculate the contractional strain as a function of time. For the *W&D* model, we find a steady increase in the contractional strain up to a value of $\sim 2.3 \times 10^{-3}$ after 4.5 Gyr. Alternately, the *L&F* model predicts an early period of global heating and volumetric expansion due to the initial high heat flux from the short-lived ^{40}K, with the net strain only becoming contractional after 400 Myr, and with a cumulative strain of approximately 2.4×10^{-3} after 4.5 Gyr. Thus the strain history predicted by these two models is quite similar after the first few hundred million years of Mars history. In contrast, the *W&D (hot)* model predicts a significantly greater contractional strain of 5.2×10^{-3} after 4.5 Gyr.

[53] In addition, to the thermal contraction as the planet cools, phase changes in the olivine-spinel system within the mantle will migrate in response to the changing potential temperature of the mantle, leading to further contraction. It is thought that the Martian mantle likely experiences both the α to β (olivine to wadsleyite) and β to γ (wadsleyite to ringwoodite) phase changes, corresponding to the 410- and 520-km seismic discontinuities on the Earth [*Breuer et al.*, 1996]. Both phase changes result in a discontinuous increase in density with depth and have positive Clapeyron slopes (e.g., are exothermic). Thus as the internal temperature of Mars decreased, the phase change boundaries would occur at lower pressures and migrate radially outward, leading to an increase in the average density of the mantle and a resulting contractional strain. These phase changes have been estimated to occur at depths of 1020 and 1360 km on Mars, as a result of the lower pressure gradient relative to the Earth [*Breuer et al.*, 1996]. The Clapeyron slopes of $\sim$3 and 5 MPa/K can be used to calculate the change in depth of the phase changes with changing temperature, and the resulting contractional strain. The contractional strain ε_{12} resulting from a shift in the radius δR_{12} of the transition from phase 1 to phase 2, characterized by a fractional density change $\delta\rho_{12} \cdot \rho_1^{-1}$ and Clapeyron slope C_{12}, and acted on by the gravitational acceleration g_{12} at radius R_{12}, is calculated as:

$$\varepsilon_{12} = 1 - \left[1 - \frac{4\pi R_{12}^2 \cdot \delta R_{12} \cdot \delta\rho_{12} \cdot \rho_1^{-1}}{{}^4/_3 \pi R_{Mars}^3}\right]^{1/3} \Bigg| \delta R_{12} \approx \frac{C_{12} \cdot \delta T}{\rho_1 g_{12}} \tag{2}$$

The effect of the adiabatic temperature change in the mantle over δR_{12} is smaller than the uncertainty in the Clapeyron slopes, and has been neglected above. We adopt values for the increase in bulk mantle density at the α to β phase transition of 2.6% [*Mayama et al.*, 2004; *Shearer and Flanagan*, 1999], and at the β to γ transition of 2.1% [*Li*, 2003]. For an average internal temperature change of 100 K, the combined effect of both phase changes will result in a global contractional strain of 1.6×10^{-4} in addition to that generated by simple thermal contraction of the mantle.

[54] It is possible that the Martian mantle also undergoes the γ ringwoodite to perovskite phase transition, corresponding to the 660 km discontinuity on the Earth, though this transition would likely only occur near the core–mantle boundary early in Mars history, if at all [*Breuer et al.*, 1996]. As a result of the negative Clapeyron slope (-3 MPa/K), inward migration of this phase transition in response to planetary cooling would drive a global expansion, though the greater depth of this phase transition would mitigate the resulting strain somewhat. Since it is unclear if or when this phase transition existed in the Martian mantle, we do not include it in our calculations. The effect of this transition would be to decrease the final theoretical contractional strain estimates by $<10^{-4}$, which would not affect the conclusions of this study.

[55] Plume-induced volcanic activity during the formation of Tharsis is another likely cause of contraction [*Tanaka et al.*, 1991]. The rise of a hot mantle plume or plumes from deep in the mantle to the base of the lithosphere would have extracted a tremendous volume of partial melt from the mantle, while advecting a significant amount of heat to the surface. The volcanic outpouring of a volume of magma equal to the estimated volume of the Tharsis load of 3×10^8 km^3 [*Phillips et al.*, 2001] would have resulted in a contractional strain of approximately 6×10^{-4} due to the simple removal of material from the interior. Extraction of a 10% partial melt from mantle material results in a decrease

in density of the mantle residuum by roughly 0.5% [*Phillips et al.*, 1990; *Niu and Batiza*, 1991], however, this effect is negligible in comparison with the uncertainty in the volume of Tharsis magmas, and we have neglected it in our calculated Tharsis-induced strain.

[56] The heat advected to the surface by the hypothesized Tharsis plume(s) depends on the volume of the mantle plume material required to form Tharsis, which can be estimated using the volume of Tharsis and assuming a partial melt fraction of 10% [*Campbell and Griffiths*, 1990; *Griffiths and Campbell*, 1990; *McKenzie and Bickle*, 1988] to be 3×10^9 km^3. This volume may be an underestimate, as partial melting is thought to be confined to the upper portions of the plume head [*Campbell and Griffiths*, 1990; *Griffiths and Campbell*, 1990]. However, the lower gravity on Mars and correspondingly reduced pressure gradient would tend to increase the thickness of the zone of partial melting in the mantle. Plume rise is thought to be driven by a mantle potential temperature difference of $\sim$500 K [*Campbell and Griffiths*, 1990]. Assuming a thermal expansivity of 3.3×10^{-5} K^{-1}, the global horizontal contractional strain resulting from the rise and conductive cooling of the plume(s) after reaching the base of the lithosphere is approximately 8×10^{-5}. An additional component of latent heat loss would result from the melting at depth followed by extrusion and solidification at the surface, though the resulting thermal contraction would be small relative to other sources [*Hauck et al.*, 2003]. The combined strain from Tharsis volcanism and plume-induced cooling is then $\sim 7 \times 10^{-4}$. While a mantle plume origin for Tharsis is speculative at this point, the global cooling in response to the advection of heat by the plume is small compared to the contraction in response to the volcanic outpouring itself, so the contractional strain resulting from alternate models of Tharsis formation would be similar.

[57] The bulk of this Tharsis-induced contraction likely occurred during the Noachian, as is suggested by evidence for an early Tharsis formation [*Anderson et al.*, 2001; *Phillips et al.*, 2001]. We add the inferred Tharsis-induced contractional strain distributed linearly over the Noachian to the time-dependent strain resulting from the secular cooling of the planet and migration of phase change boundaries, and compare the resulting strain history with the values inferred from the ages and locations of the Memnonia and Amazonis strike-slip faults (Figure 12). The theoretical strain history for the *W&D (hot)* model agrees well with the predictions based on the strike-slip faults for lithosphere thicknesses between 35 and 50 km. The contractional strains inferred from the strike-slip faults for the 100-km-thick lithosphere agree well with the strain histories based on the *W&D* and *L&F* models. In contrast, for thicker and thinner lithospheres, the strike-slip faults under- and overpredict the strains, respectively. The 200-km-thick lithosphere predicts much lower strains during the Late Hesperian to Early Amazonian than any of the thermal models. Furthermore, these contractional strains are significantly lower than the strains inferred from the wrinkle ridges [*Golombek et al.*, 2001]. Similarly, the strains inferred from the faults for a 25-km-thick lithosphere exceed the strains from all of the thermal models during the Late Hesperian to Early Amazonian, and the strains for a 10-km-thick lithosphere would plot off the chart.

[58] Thus comparison of the strains inferred from the strike-slip faults with the theoretically predicted contractional strain history from thermal models allows us to constrain the mean lithosphere thickness at the time of Tharsis formation to have been between 35 and 100 km, depending on the initial thermal state of Mars. For lithosphere thicknesses between 35 and 50 km, the contractional strain history inferred from the strike-slip faults requires a source of rapid contraction early in Mars history, consistent with a hot early Mars, as well as a thick enough lithosphere to record that early rapid contraction. These two requirements may be contradictory, as the high temperatures and heat fluxes would imply a thin lithosphere incapable of withstanding such large contractional stresses without failing. Another possible source of early rapid contraction is the growth of a solid inner core early in Mars history, though a solid inner core is difficult to reconcile with both evidence for a liquid outer core on Mars today and the present-day lack of a magnetic field [*Stevenson*, 2001]. Furthermore, the 35–50 km lithosphere models were found in section 3.2 to predict strike-slip faulting to be much more widespread than the observed distribution of faults (Figure 11). The limited distribution of strike-slip faults was found to be most consistent with a lithosphere thickness at the time of Tharsis formation of approximately 100 km, which agrees best with the thermal evolution based on a cool early Mars. Thus the contractional strain evolution predicted on the basis of the history of strike-slip faulting suggests that either Mars did not undergo a period of rapid early cooling and contraction, or that the thin early lithosphere was incapable of maintaining the resulting contractional stresses, and so they did not affect the subsequent tectonic evolution.

4. Conclusions

[59] The tectonic record of Mars is preserved in populations of graben, wrinkle ridges, and strike-slip faults, primarily focused around the Tharsis region. We have presented evidence for a new population of Noachian to Early Hesperian-aged potential strike-slip faults southwest of Tharsis. These Memnonia strike-slip faults represent the oldest strike-slip faults identified on Mars, and the only case in which the large-scale lateral offset across a fault has been clearly documented. A strike-slip interpretation for these faults is supported by evidence for transverse horizontal displacement and asymmetric vertical throw in two of the best-preserved faults, as well as the linearity and orientations of the entire population of faults relative to the regional principal stress directions. While much of the evidence supporting the strike-slip nature of these ancient faults is circumstantial, all available evidence to date supports this interpretation. Future work will likely strengthen the interpretation for some faults, refute others, and continue identify previously undocumented faults in this region.

[60] The tectonic evolution of Mars has been dominated by the interaction of the membrane-flexural stresses induced by Tharsis loading and the global contractional stresses. In consideration of the superposition of these two stress fields, we have shown that the predicted styles of faulting differ substantially from those based on loading alone, with large areas of the planet having experienced stresses conducive to strike-slip faulting for portions of their history. Regions of

predicted strike-slip faulting to the west of Tharsis coincide with previously mapped Late Hesperian-Early Amazonian strike-slip faults northwest of Tharsis, and the newly identified group of Noachian–Early Hesperian strike-slip faults southwest of Tharsis.

[61] As a transitional state during the tectonic evolution of a given area that is uniquely diagnostic of the orientations of all three principal stress vectors, strike-slip faulting provides the strongest constraint on the tectonic and geodynamic history of Mars. Comparison of the ages and locations of the two groups of strike-slip faults to the predictions of the loading and contractional models allows us to place constraints on the evolving stress and strain state of Mars. The resulting contractional strain history agrees well with theoretical strain predictions based on the secular cooling of the planet throughout Mars history, augmented by plume-induced cooling and melt extraction beneath Tharsis during the Noachian.

[62] Using the range of contractional strains predicted from thermal evolution models, we constrain the lithosphere thickness at the time of Tharsis loading to have been between 35 and 100 km. Comparison of the predicted deviatoric stresses with the critical stresses required for faulting shows that the observed distribution of strike-slip faults is most consistent with a lithosphere thickness at the time of Tharsis loading of approximately 100 km. The strains inferred from the strike-slip faults for a 100-km-thick lithosphere agree well with thermal evolution models in which early Mars was comparatively cool, or did not possess a sufficiently strong lithosphere to preserve the record of an early period of rapid cooling. This work also allows us to predict the stress state and predicted style of tectonism for other regions of the planet and at other times in Mars history. Further refinements to the stress and strain history of Mars will be possible as we improve our understanding of the tectonic history.

[63] Among the terrestrial planets, Mars is particularly amenable to the study of its internal and geodynamic evolution over the entire history of the planet. While Venus and the Earth show abundant evidence of geologic and tectonic activity, their surfaces are comparatively young and do not preserve the record of the earliest periods of the planets' evolution. Mercury and the Moon, on the other hand, have ancient surfaces, though they show much less evidence of geologic activity than the larger terrestrial planets. Mars alone possesses both an ancient surface, much of which dates back to the heavy bombardment, and evidence for a dynamic history of volcanism, loading, and tectonism. This work suggests that strike-slip faults, which have received little attention in the literature until recently, may be the key to unraveling Mars' tectonic, geodynamic, and thermal evolution.

[64] **Acknowledgments.** We are especially grateful to Bruce Banerdt for the use of his thin-shell code. We would like to thank Mindi Searls for useful discussions that contributed to this work. This manuscript benefited from thorough reviews by Bruce Banerdt and an anonymous reviewer. This work was supported in part by a NASA Planetary Geology and Geophysics Program grant to M.T.Z.

References

Anderson, R. C., J. M. Dohm, M. P. Golombek, A. F. C. Haldemann, B. J. Franklin, K. L. Tanaka, J. Lias, and B. Peer (2001), Primary centers and secondary concentrations of tectonic activity through time in the western hemisphere of Mars, *J. Geophys. Res.*, *106*(E9), 20,563–20,585.

Anguita, F., A.-F. Farelo, V. Lopez, C. Mas, M.-J. Munoz-Espadas, A. Marquez, and J. Ruiz (2001), Tharsis dome, Mars: New evidence for Noachian–Hesperian thick-skin and Amazonian thin-skin tectonics, *J. Geophys. Res.*, *106*(E4), 7577–7589.

Artita, K. S., and R. A. Schultz (2005), Significance of deformation band-like strike-slip faults on Mars, *Lun. Plan. Sci.*, *XXXVI*, abstract 2225.

Banerdt, W. B. (1986), Support of long-wavelength loads on Venus and implications for internal structure, *J. Geophys. Res.*, *91*(B1), 403–419.

Banerdt, W. B., and M. P. Golombek (2000), Tectonics of the Tharsis region of Mars: Insights from MGS topography and gravity, *Lun. Plan. Sci.*, *XXXI*, abstract 2038.

Banerdt, W. B., R. J. Phillips, N. H. Sleep, and R. S. Saunders (1982), Thick shell teconics on one-plate planets: Applications to Mars, *J. Geophys. Res.*, *87*(B12), 9723–9733.

Banerdt, W. B., M. P. Golombek, and K. L. Tanaka (1992), Stress and tectonics on Mars, in *Mars*, edited by W. S. Kiefer, pp. 249–297, University of Arizona Press, Tucson.

Breuer, D., H. Zhou, D. A. Yuen, and T. Spohn (1996), Phase transitions in the Martian mantle: Implications for the planets volcanic history, *J. Geophys. Res.*, *101*(E3), 7531–7542.

Campbell, I. H., and R. W. Griffiths (1990), Implications of mantle plume structure for the evolution of flood basalts, *Earth Planet. Sci. Lett.*, *99*, 79–93.

Carr, M. H. (1974), Tectonism and volcanism of the Tharsis region of Mars, *J. Geophys. Res.*, *79*, 3943–3949.

Dohm, J. M., and K. L. Tanaka (1999), Geology of the Thaumasia region, Mars: Plateau development, valley origins, and magmatic evolution, *Planet. Space Sci.*, *47*, 411–431.

Einarsson, P., and J. Eiriksson (1982), Earthquake fractures in the districts Land and Rangarvellir in the South Iceland Seismic Zone, *Jokull*, *32*, 113–119.

Elkins-Tanton, L. T., P. C. Hess, and E. M. Parmentier (2005), Possible formation of ancient crust on Mars through magma ocean processes, *J. Geophys. Res.*, *110*(E12), E12S01, doi:10.1029/2005JE002480.

Ernst, R. E., E. B. Grosfils, and D. Mege (2001), Giant dike swarms: Earth, venus, and mars, *Ann. Rev. Earth Planet. Sci.*, *29*, 489–534.

Fei, Y. (1995), Thermal expansion, in *Mineral Physics and Crystallography: A Handbook of Physical Constants*, edited by T. J. Ahrens, pp. 354, AGU, Washington, D. C.

Forsythe, R. D., and J. R. Zimbelman (1989), Is the Gordii Dorsum escarpment on Mars an exhumed transcurrent fault?, *Nature*, *336*, 143–146.

Golombek, M. P. (1985), Fault type predictions from stress distributions on planetary surfaces: Importance of fault initiation at depth, *J. Geophys. Res.*, *90*(B4), 3065–3074.

Golombek, M. P., F. S. Anderson, and M. T. Zuber (2001), Martian wrinkle ridge topography: Evidence for subsurface faults from MOLA, *J. Geophys. Res.*, *106*, 23,811–23,821.

Golombek, M. P., J. A. Grant, L. S. Crumpler, R. E. Arvidson, J. F. Bell, C. M. Weitz, R. J. Sullivan, P. R. Christensen, L. A. Soderblom, and S. W. Squyres (2006), Erosion rates at the Mars Exploration Rover landing sites and long-term climate change on Mars, *J. Geophys. Res.*, *111*, E12S10, doi:10.1029/2006JE002754.

Griffiths, R. W., and I. H. Campbell (1990), Stirring and structure in mantle starting plumes, *Earth Planet. Sci. Lett.*, *99*, 66–78.

Grott, M., and D. Breuer (2008), The evolution of the Martian elastic lithosphere and implications for crustal and mantle rheology, *Icarus*, *193*, 503–515.

Hanna, J. C., and R. J. Phillips (2006), Tectonic pressurization of aquifers in the formation of Mangala and Athabasca Valles, Mars, *J. Geophys. Res.*, *111*, E03003, doi:10.1029/2005JE002546.

Hartmann, W. K., and G. Neukum (2001), Cratering chronology and the evolution of Mars, *Space Sci. Rev.*, *96*, 165–194.

Hartmann, W. K., J. Anguita, M. A. de la Casa, D. C. Berman, and E. V. Ryan (2001), Martian cratering 7: The role of impact gardening, *Icarus*, *149*, 37–53.

Hauber, E., E. Charalambakis, K. Gwinner, M. Knapmeyer, and M. Grott (2007), Displacement-length relationships of normal faults on Mars: New observations with MOLA and HRSC, *7th Int. Conf. Mars*, Abstract 3110.

Hauck, S. A., and R. J. Phillips (2002), Thermal and crustal evolution of Mars, *J. Geophys. Res.*, *107*(E7), 5052, doi:10.1029/2001JE001801.

Hauck, S. A., S. C. Solomon, and R. J. Phillips (2003), Potential sources of contractional tectonics on Mars, *Lun. Plan. Sci.*, *XXXIV*, abstract 1667.

Head, J. W., M. A. Kreslavsky, and S. Pratt (2002), Northern lowands of Mars: Evidence for widespread volcanic flooding and tectonic deformation in the Hesperian Period, *J. Geophys. Res.*, *107*(E1), 5003, doi:10.1029/2000JE001445.

Hoek, E., and E. T. Brown (1980), Empirical strength criterion for rock masses, *J. Geotech. Eng. Div. Am. Soc. Civ. Eng.*, *106*, 1013–1035.

Jaeger, W. L., L. P. Keszthelyi, A. S. McEwen, C. M. Dundas, and P. S. Russell (2007), Athabasca Valles, Mars: A lava-draped channel system, *Science*, *317*, 1709–1711.

Lee, D.-C., and A. N. Halliday (1997), Core formation on Mars and differentiated asteroids, *Nature*, *388*, 854–857.

Li, B. (2003), Compressional and shear wave velocities of ringwoodite gamma-Mg2SiO4 to 12 GPa, *Am. Mineral.*, *88*, 1312–1317.

Lodders, K., and B. Fegley (1997), An oxygen isotope model for the composition of Mars, *Icarus*, *126*, 373–394.

Mayama, N., I. Suzuki, T. Saito, I. Ohno, T. Katsura, and A. Yoneda (2004), Temperature dependence of elastic moduli in β-$(Mg, Fe)_2SiO_4$, *Geophys. Res. Lett.*, *41*(4), L04612, doi:10.1029/2003GL019247.

McGovern, P. J., S. C. Solomon, D. E. Smith, M. T. Zuber, M. Simons, M. A. Wieczorek, R. J. Phillips, G. A. Neumann, O. Aharonson, and J. W. Head (2002), Localized gravity/topography admittance and correlation spectra on Mars: Implications for regional and global evolution.

McGovern, P. J., S. C. Solomon, D. E. Smith, M. T. Zuber, M. Simons, M. A. Wieczorek, R. J. Phillips, G. A. Neumann, O. Aharonson, and J. W. Head (2004), Correction to "Localized gravity/topography admittances and correlation spectra on Mars: Implications for regional and global evolution", *J. Geophys. Res.*, *109*, E07007, doi:10.1029/2004JE002286.

McKenzie, D., and M. J. Bickle (1988), The volume and composition of melt generated by extension of the lithosphere, *J. Geophys. Res.*, *89*(B13), 11,180–11,194.

McNutt, M. K. (1984), Lithospheric flexure and thermal anomalies, *J. Geophys. Res.*, *89*(B13), 11,180–11,194.

Mohit, P. S., and J. Arkani-Hamed (2004), Impact demagnetization of the Martian crust, *Icarus*, *168*(2), 305–317.

Mount, V. S., and J. Suppe (1987), State of stress near the San Andreas fault: Implications for wrench tectonics, *Geology*, *15*, 1143–1146.

Naylor, M. A., G. Mandl, and C. H. Sijpesteijn (1986), Fault geometries in basement-induced wrench faulting under different initial stress states, *J. Struct. Geol.*, *8*, 737–752.

Neumann, G. A., M. T. Zuber, M. A. Wieczorek, P. J. McGovern, F. G. Lemoine, and D. E. Smith (2004), Crustal structure of Mars from gravity and topography, *J. Geophys. Res.*, *109*, E08002, doi:10.1029/2004JE002262.

Nimmo, F., and M. S. Gilmore (2001), Constraints on the depth of the magnetized crust on Mars from impact craters, *J. Geophys. Res.*, *106*(E6), 12,315–12,324.

Niu, Y., and R. Batiza (1991), In situ densities of MORB melts and residual mantle: Implications for buoyancy forces beneath mid-ocean ridges, *J. Geol.*, *99*(767–775).

Okubo, C. H., and A. S. McEwen (2007), Fracture-controlled paleo-fluid flow in Candor Chasma, Mars, *Science*, *315*, 983–985.

Okubo, C. H., and R. A. Schultz (2006), Variability in Early Amazonian Tharsis stress state based on wrinkle ridges and strike-slip faulting, *J. Struct. Geol.*, *28*, 2169–2181.

Okubo, C. H., and the HiRISE Team (2007), Deformation bands on Mars and implications for subsurface fluid flow, *7th Int. Conf. Mars*, abstract 3041.

Phillips, R. J., N. H. Sleep, and W. B. Banerdt (1990), Permanent uplift in magmatic systems with application to the Tharsis region of Mars, *J. Geophys. Res.*, *95*(B4), 5089–5100.

Phillips, R. J., et al. (2001), Ancient geodynamics and global-scale hydrology on Mars, *Science*, *291*, 2587–2591.

Plescia, J. B., and R. S. Saunders (1982), Tectonic history of the Tharsis region, Mars, *J. Geophys. Res.*, *87*(B12), 9775–9791.

Scholz, C. H. (2000), Evidence for a strong San Andreas fault, *Geology*, *28*, 163–166.

Scholz, C. H. (2002), *The Mechanics of Earthquakes and Faulting*, 471 pp., Cambridge University Press, Cambridge.

Schubert, G., and T. Spohn (1990), Thermal history of Mars and the sulfur content of its core, *J. Geophys. Res.*, *95*, 14,095–14,104.

Schultz, R. A. (1989), Strike-slip faulting of ridged plains near Valles Marineris, Mars, *Nature*, *341*, 424–426.

Schultz, R. A., and M. T. Zuber (1994), Observations, models, and mechanisms of failure of surface rocks surrounding planetary loads, *J.Geophys. Res.*, *99*(E7), 14,691–14,702.

Schultz, R. A., C. H. Okubo, C. L. Goudy, and S. J. Wilkins (2004a), Igneous dikes on Mars revealed by Mars Orbiter Laser Altimeter topography, *Geology*, *32*(10), 889–892.

Schultz, R. A., C. H. Okubo, and S. J. Wilkins (2004b), Displacement-length scaling of faults on Earth, Mars, and beyond, *Lun. Plan. Sci.*, *35*, Abstract 1157.

Shearer, M. P., and P. M. Flanagan (1999), A map of topography on the 410-km discontinuity from PP precursors, *Geophys. Res. Lett.*, *26*(5), 549–552.

Sleep, N. H. (1994), Martian plate tectonics, *J. Geophys. Res.*, *99*(E3), 5639–5655.

Sleep, N. H., and R. J. Phillips (1985), Gravity and lithospheric stress on the terrestrial planets with reference to the Tharsis region of Mars, *J. Geophys. Res.*, *90*, 4469–4489.

Smith, D. E., W. L. Sjorgren, G. L. Tyler, G. Balmino, and F. G. Lemoine (1999a), The gravity field of Mars: Results from the Mars Global Surveyor, *Science*, *286*, 94–96.

Smith, D. E., et al. (1999b), The global topography of Mars and implications for surface evolution, *Science*, *284*, 1495–1503.

Smith, D. E., et al. (2001), Mars Orbiter Laser Altimeter (MOLA): Experiment summary after the first year of global mapping of Mars, *J. Geophys. Res.*, *106*, 23,689–23,722.

Stevenson, D. J. (2001), Mars' core and magnetism, *Nature*, *412*, 214–219.

Tanaka, K. L., M. P. Golombek, and W. B. Banerrdt (1991), Reconciliation of stress and structural histories of the Tharsis region of Mars, *J. Geophys. Res.*, *96*(E1), 15,617–15,633.

Tanaka, K. L., J. A. Skinner, T. M. Hare, T. Joyal, and A. Wenker (2003), Resurfacing history of the northern plains of Mars based on geologic mapping of Mars Global Surveyor data, *J. Geophys. Res.*, *108*(E4), 8043, doi:10.1029/2002JE001908.

ten Brink, U. S., R. Katzman, and J. Lin (1996), Three-dimensional model of deformation near strike-slip faults, *J. Geophys. Res.*, *101*, 16,205–16,220.

Vlasov, V. Z. (1964), *General Theory of Shells and Its Applications in Engineering*, 886 pp., NASA Tech. Trans. T T F-99.

Wänke, H., and G. Dreibus (1994), Chemistry and accretion of Mars, *Philos. Trans. R. Soc. London, Ser. A*, *349*, 2134–2137.

Watters, T. R. (1993), Compressional tectonism on Mars, *J. Geophys. Res.*, *98*(E9), 17,049–17,060.

Wieczorek, M. A., and M. T. Zuber (2004), Thickness of the Martian crust: Improved constraints from geoid-to-topography ratios, *J. Geophys. Res.*, *109*, E01009, doi:10.1029/2003JE002153.

Wilson, L., and J. W. Head (2002), Tharsis-radial graben systems as the surface manifestations of plume-related dike intrusion complexes: Models and implications, *J. Geophys. Res.*, *107*(E4), 5019, doi:10.1029/2000JE001431.

Zuber, M. T., et al. (2000), Internal structure and early thermal evolution of Mars from Mars Global Surveyor topography and gravity, *Science*, *287*, 1788–1793.

J. C. Andrews-Hanna and M. T. Zuber, Department of Earth, Atmospheric, and Planetary Sciences, Massachusetts Institute of Technology, Cambridge, MA 02139, USA. (jhanna@mit.edu)

S. A. Hauck II, Department of Geological Sciences, Case Western Reserve University, 10900 Euclid Ave, Cleveland, OH 44106, USA.